

# Biomimetic Trypsin-Responsive Structure-Bridged Mesoporous Organosilica Nanomedicine for Precise Treatment of Acute Pancreatitis

Yanan Wang,<sup>||</sup> Deyao Qian,<sup>||</sup> Xinyuan Wang, Xue Zhang, Zerui Li, Xinlei Meng, Liangmin Yu, Xuefeng Yan, and Zhiyu He\*

Cite This: <https://doi.org/10.1021/acsnano.4c05369>

Read Online

ACCESS |

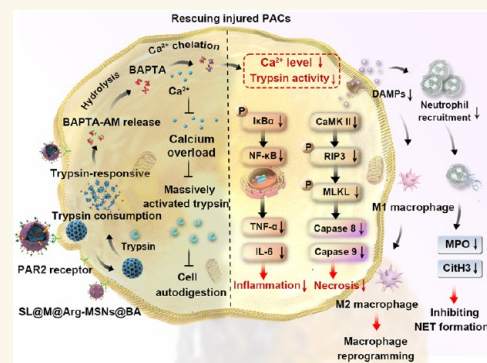
Metrics & More

Article Recommendations

Supporting Information

**ABSTRACT:** Developing strategies to target injured pancreatic acinar cells (PACs) in conjunction with primary pathophysiology-specific pharmacological therapy presents a challenge in the management of acute pancreatitis (AP). We designed and synthesized a trypsin-cleavable organosilica precursor bridged by arginine-based amide bonds, leveraging trypsin's ability to selectively identify guanidino groups on arginine via Asp189 at the active S1 pocket and cleave the carboxy-terminal (C-terminal) amide bond via catalytic triads. The precursors were incorporated into the framework of mesoporous silica nanoparticles (MSNs) for encapsulating the membrane-permeable  $\text{Ca}^{2+}$  chelator BAPTA-AM with a high loading content (~43.9%). Mesenchymal stem cell membrane coating and surface modification with PAC-targeting ligands endow MSNs with inflammation recruitment and precise PAC-targeting abilities, resulting in the highest distribution at 3 h in the pancreas with 4.7-fold more accumulation than that of naked MSNs. The outcomes transpired as follows: After bioinspired MSNs' skeleton biodegradation by prematurely and massively activated trypsin, BAPTA-AM was on-demand released in injured PACs, thereby effectively eliminating intracellular calcium overload (reduced  $\text{Ca}^{2+}$  level by 81.3%), restoring cellular redox status, blocking inflammatory cascades, and inhibiting cell necrosis by impeding the  $\text{I}\kappa\text{B}\alpha/\text{NF-}\kappa\text{B}/\text{TNF-}\alpha/\text{IL-6}$  and  $\text{CaMK-II}/\text{p-RIP3}/\text{p-MLKL}/\text{caspase-8,9}$  signaling pathways. In AP mice, a single dose of the formulation significantly restored pancreatic function (lipase and amylase reduced more by 60%) and improved the survival rate from 50 to 91.6%. The formulation offers a potentially effective strategy for clinical translation in AP treatment.

**KEYWORDS:** acute pancreatitis, acinar cell targeting, BAPTA-AM, mesoporous silica nanoparticles, trypsin-responsive



## INTRODUCTION

Severe acute pancreatitis (AP), a severe acute inflammatory disease, is one of the most common gastrointestinal diseases encountered in the emergency department and is associated with a high mortality rate (40%).<sup>1–3</sup> The findings of randomized clinical trials on AP pharmacotherapy have been limited, and there are still no specific and targeted therapies available for AP in clinical applications.<sup>4,5</sup>

The primary cause of AP is intracellular calcium overload and premature and massive trypsin activation, resulting in autodigestion of pancreatic acinar cells (PACs) and then provokes oxidative stress injury, pancreatic and peripancreatic necrosis, systemic inflammatory response syndrome, and even multiple organ failure.<sup>6–10</sup> However, the currently available pancreas-protective drugs only target one aspect of the

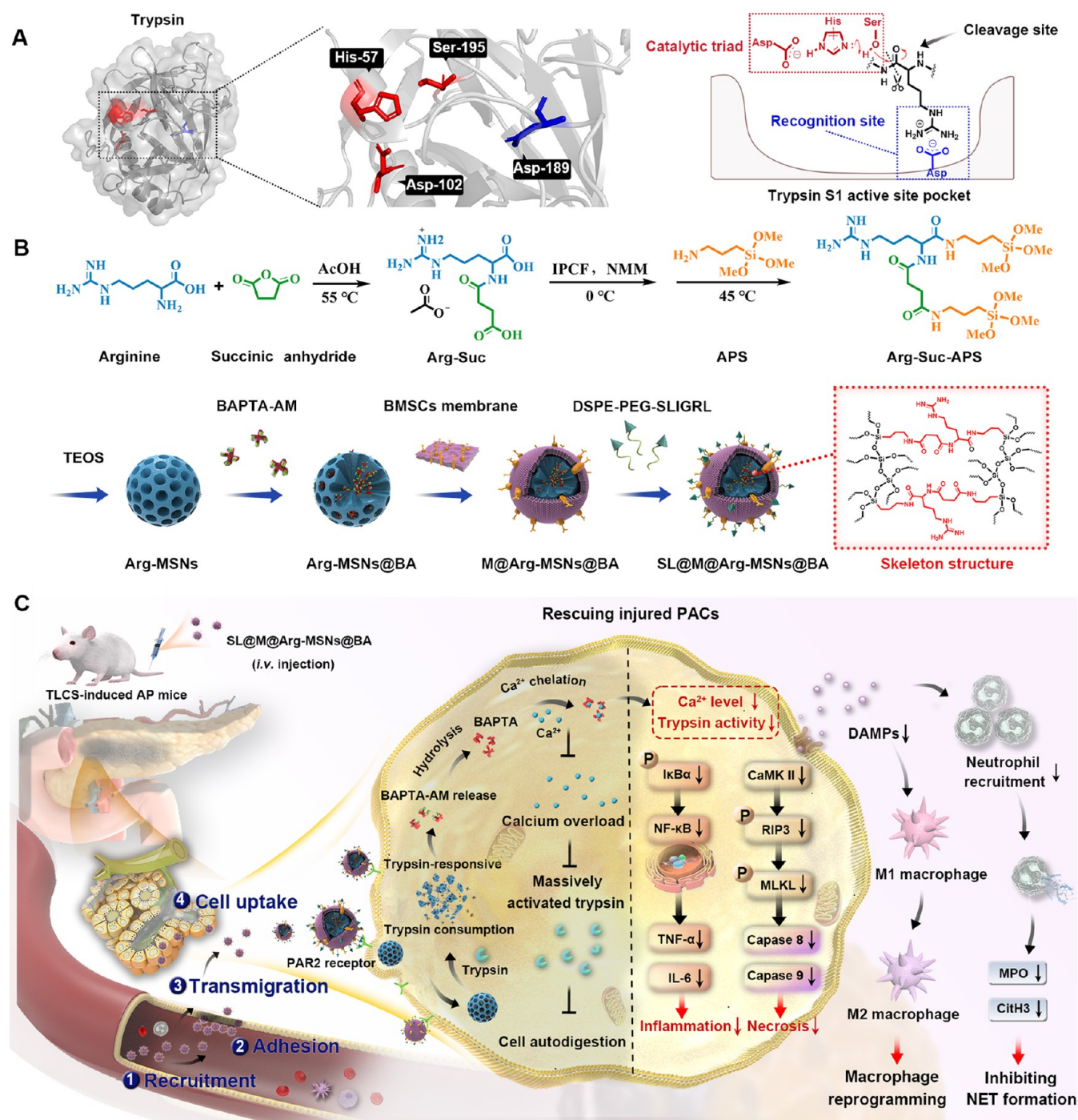
downstream pathophysiological pathways, making it challenging to reverse the two main drivers of pathology from the root.<sup>11–14</sup> Additionally, their treatment efficiencies are limited by a short half-life, poor drug water solubility, a lack of pancreas-targeting ability resulting from the deep pancreatic anatomical position, the existence of the blood pancreatic barrier (BPB), and limited PACs' targeting receptors.<sup>15</sup> Diverse drug delivery systems (DDS) for pancreas-targeting, such as

Received: April 23, 2024

Revised: June 28, 2024

Accepted: July 1, 2024

Scheme 1. Schematic Representation Depicting (A) the Substrate Recognition Site and Structure of Catalytic Triad of Trypsin and Its Substrate Degradation Mechanism, (B) the Preparation of SL@Arg-MSNs@BA and (C) Its Therapeutic Mechanism in a Mouse Model of Acute Pancreatitis Induced by Sodium Taurocholate Retrograde Infusion



inflammation-targeted DDS, are limited to the pancreatic inflammation region but lack selectivity for specific damaged cells within the pancreas.<sup>16–19</sup> Furthermore, pathological microenvironment-responsive DDS for delivery to the pancreas, such as ROS- and pH-triggered systems, remained unsatisfactory in AP therapy because increased oxidative stress and low pH are not the primary pathological features at the early stages of pancreatic injury.<sup>20–22</sup> This leads to an inevitable lack of control over drug-release patterns, which results in either an unfavorable premature release of drugs in nontarget organs or a delayed release at the core tissue injury

lesion, thereby undermining therapeutic effectiveness.<sup>23,24</sup> To initiate comprehensive treatment by reversing upstream calcium overload and trypsin activation-mediated pancreatic autodigestion and restoring pancreatic function, it is necessary to develop strategies that target specific PACs and deliver drugs in a precise and rapid manner in response to the injured pancreas' core microenvironment.

Trypsin is a serine protease with an active S1 catalytic pocket that exhibits a highly specific cleavage affinity for the carboxy-terminal (C-terminal) amide bond formed by a basic residue (lysine (Lys) or arginine (Arg)). The carboxylate

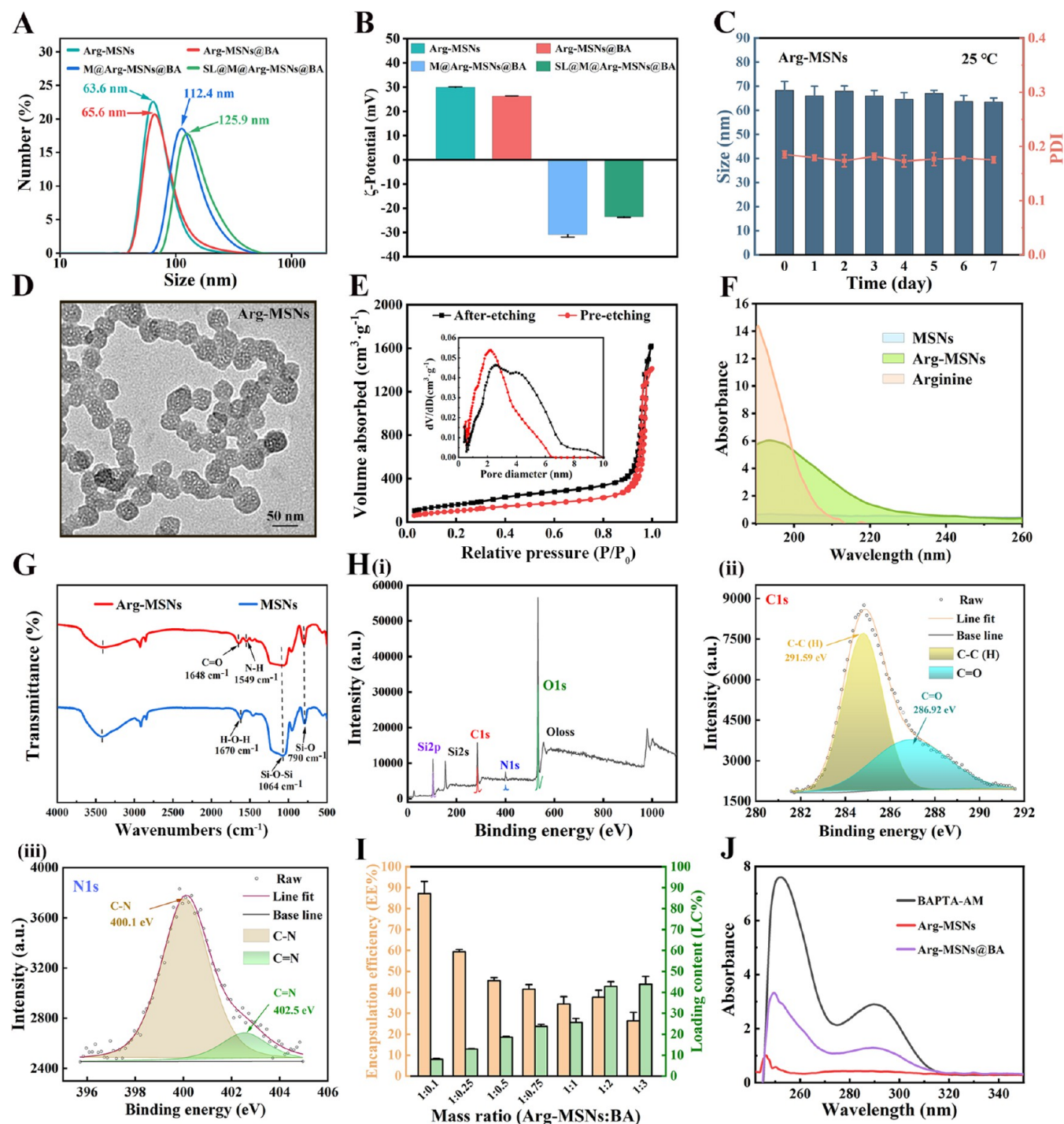


**Figure 1.** Characteristics of the Arg-MSNs. (A) The particle size and (B)  $\zeta$ -potential of Arg-MSNs, Arg-MSNs@BA, M@Arg-MSNs@BA, and SL@M@Arg-MSNs@BA. (C) The stability of Arg-MSNs. (D) Representative TEM images of Arg-MSNs. (E)  $N_2$  adsorption isotherms of Arg-MSNs. (F) UV-vis absorption spectra of MSNs, Arg, and Arg-MSNs. (G) The Fourier transform infrared (FTIR) spectra of MSNs and Arg-MSNs. (H) (i) X-ray photoelectron spectroscopy (XPS) spectra of Arg-MSNs, (ii) peak-fitting of C 1s, and (iii) peak-fitting of N 1s. (I) The percent of encapsulation efficiency (EE) and drug loading content (LC) of BA in Arg-MSNs. (J) UV-vis absorption spectra of BAPTA-AM, Arg-MSNs, and Arg-MSNs@BA in dimethyl sulfoxide (DMSO).

groups on Asp189's side chains, situated at the bottom of the S1 pocket, could facilitate the formation of a salt bridge with the positively charged guanidino groups on Arg, and this interaction strengthens the binding of substances with trypsin.<sup>25,26</sup> Therefore, the Arg-derived amide bond structure has the potential for rapid recognition, robust binding, and degradation by trypsin.

Mesoporous silica nanoparticles (MSNs) have attracted significant interest due to their customizable surface functionalization, tunable pore size for high drug loading, and the feasibility of introducing microenvironment-responsive elements into skeletons, allowing for the desired controlled release mechanism via matrix degradation.<sup>27–32</sup> Given that trypsin overproduction is one of the earliest and most typical

features of PAC damage, our hypothesis incorporates trypsin-reactive and cleavable Arg-based organosilica moieties with functional amide bond elements at the backbone of the MSNs. Our goal is to produce organo-bridged MSNs that undergo self-destructive pathways, enabling the rapid and precise release of cargo molecules in response to massively activated trypsin in injured PACs.

We designed and synthesized an organosilica precursor containing a trypsin-cleavable Arg-based amide bond. The precursor was incorporated into the framework of mesoporous silica to create trypsin-responsive organo-bridged MSNs (Arg-MSNs) for the effective encapsulation of a membrane-permeable calcium chelator 1,2-bis(2-aminophenoxy)ethane-*N,N,N,N'*-tetraacetic acid (BAPTA-AM, BA) to produce Arg-MSNs@BA, aiming for controlled drug release and rapidly eliminating the intracellular overloaded  $\text{Ca}^{2+}$  during the early stages of AP.<sup>33–38</sup> The Arg-MSNs@BA would be coated with a cell membrane derived from bone marrow mesenchymal stem cells (BMSCs) and modified with a PACs targeting peptide (SLIGRL, SL) to construct bioinspired nanoparticles (SL@M@Arg-MSNs@BA) capable of immune evasion, inflammatory endothelial adhesion, trans-endothelial migration, and precise targeting of injured cells.<sup>39–41</sup> Membrane-camouflaged NPs would rapidly recruit to the inflammatory endothelium, then target and anchor to PACs by binding the SL to the protease-activated receptor-2 (PAR2), which is largely present at the apical of PACs (Scheme 1). Following PAC internalization mediated by the biomimetic membrane layer, the core Arg-MSNs@BA would rapidly and directly biodegrade their backbone in response to prematurely and massively activated trypsin, allowing for flexible payload release. The released BA would fundamentally and efficiently chelate overloaded  $\text{Ca}^{2+}$ , addressing both symptoms and underlying causes of AP by mechanisms, such as regulating intracellular ion homeostasis, restoring cell redox status, inhibiting the pathophysiological cascade of cell apoptosis and necrosis, remodeling the imbalanced inflammatory microenvironment, reducing pancreatic tissue damage, and avoiding severe distant organ damage. The Arg-MSNs would further prevent acinar cell autodigestion by competitively consuming trypsin. Therefore, our biomimetic nanomedicine might theoretically provide comprehensive, synergistic, and multifaceted strategies by flexibly integrating overloaded calcium elimination and trypsin activity inhibition, with a huge potential for improving AP treatment outcomes.

## RESULTS AND DISCUSSION

**Synthesis and Characterization of Arg-MSNs.** The organic bridging precursor Arg-Suc-APS blocks were synthesized using a cross-linking and conjugation approach (amidation reaction), with succinic anhydride serving as a linker to anchor 3-(aminopropyl)trimethoxysilane (APTMS) units at opposite ends of the basic amino acids (Arg) (Figures S1–S4). Following that, organosilica nanoparticles (NPs) were produced using sol–gel processes that entailed the co-condensation of Arg-Suc-APS blocks and tetraethyl orthosilicate (TEOS) as coprecursors, with cetyltrimethylammonium bromide (CTAB) serving as the structure-directing agent and triethanolamine (TEAH<sub>3</sub>) acting as an alkaline catalyst, allowing for the covalent embedding of Arg-connected amide bonds into the silica framework of the organo-bridged MSNs. The as-prepared Arg-MSNs exhibited a small size (~64.0 nm), uniform size distribution (PDI: 0.182), positive surface charge

( $\zeta$ -potential: +29.8 mV), and excellent storage stability (stable at 25 °C for over 7 days) (Figure 1A–C). The transmission electron microscopy (TEM) results revealed a nearly monodispersed size distribution with an average diameter of  $48.8 \pm 6.2$  nm and a spherical morphology characterized by radially aligned mesopores on the surface (Figure 1D). The diameter of Arg-MSNs determined by TEM was ~15 nm smaller than the hydration radius observed by dynamic light scattering (DLS), which is consistent with previous findings.<sup>42</sup> Fluorescently labeled NPs with particle sizes of around 65 nm were used to assess *in vivo* biodistribution and cellular uptake (Figure S5).

As shown in Figure S6A, the X-ray diffraction (XRD) pattern of both Arg-MSNs and MSNs showed a broad diffraction peak ranging from 15 to 30°, indicating the presence of amorphous silica. The small-angle X-ray scattering (SAXS) pattern revealed a distinct and sharp scattering peak at  $2\theta = 0.46^\circ$  and a weak diffraction peak at  $2\theta = 1.59^\circ$ , confirming mesoporous structures in the Arg-MSNs, while the corresponding interplanar spacing was determined to be 19.44 and 5.52 nm, respectively (Figure S6B). Arg-MSNs have a less intense and slightly broader diffraction peak at  $2\theta = 1.52^\circ$  compared to MSNs, indicating that the introduction of the bulky Arg-based organic linker (Arg-Suc-APS) induced a slight change in the distance between the pore centers. Nitrogen adsorption–desorption plots of Arg-MSNs exhibited representative type-IV isotherms, revealing typical mesoporous structures with a specific surface area and total pore volume, and the pore sizes were calculated to be  $396.0 \text{ m}^2 \cdot \text{g}^{-1}$ ,  $1.406 \text{ cm}^3 \cdot \text{g}^{-1}$ , and ~2.6 nm based on Brunauer–Emmett–Teller (BET) (Figure 1E). The UV–vis absorption spectra of Arg-MSNs in aqueous solution revealed a characteristic absorption band of Arg at approximately 195 nm, which was close to the peak of pure Arg, indicating the incorporation of the Arg structure (Figure 1F). Fourier transform infrared (FTIR) spectroscopy revealed a transmission band at 1648 and 1549  $\text{cm}^{-1}$ , which can be assigned to the stretching vibrations of C=O and the bending vibrations of the N–H in the silicate framework, respectively, demonstrating the presence of organic functional Arg-based amide bonds in the MSN framework (Figure 1G). X-ray photoelectron spectroscopy (XPS) and scanning electron microscopy (SEM)-based elemental mapping were employed to analyze the chemical states and elemental distribution of Arg-MSNs, which confirmed the existence of Si, O, C, and N elements, which were found to be evenly distributed in the NPs (Figures 1H–i and S7). The C 1s XPS spectrum is deconvoluted into the two main peaks at 286.9 and 291.5 eV, which correspond to C=O and C–C (H) bonds, respectively (Figure 1H–ii). Besides, the N 1s spectrum, with peaks at 400.1 and 402.5 eV, supports Arg's C–N and C=N bonds (Figure 1H–iii). Both results indicated that Arg-MSNs have a typical MSN structure and multiple bonding configurations with amide bond-centered frameworks, implying that the Arg-Suc-APS blocks were successfully condensed into the organic silica framework.

Another important role of the proposed Arg-MSNs is to achieve effective encapsulation and controlled drug delivery. As shown in Figure 1I, the loading content (LC) of BA rose as the mass ratio of Arg-MSNs to BA decreased from 1:0.1 to 1:3, eventually reaching a plateau of approximately 43.9% at a ratio of 1:3. The UV–vis absorption spectra of Arg-MSNs@BA in DMSO exhibited characteristic absorption bands at approximately 289 nm, which were close to BA's absorption peak and

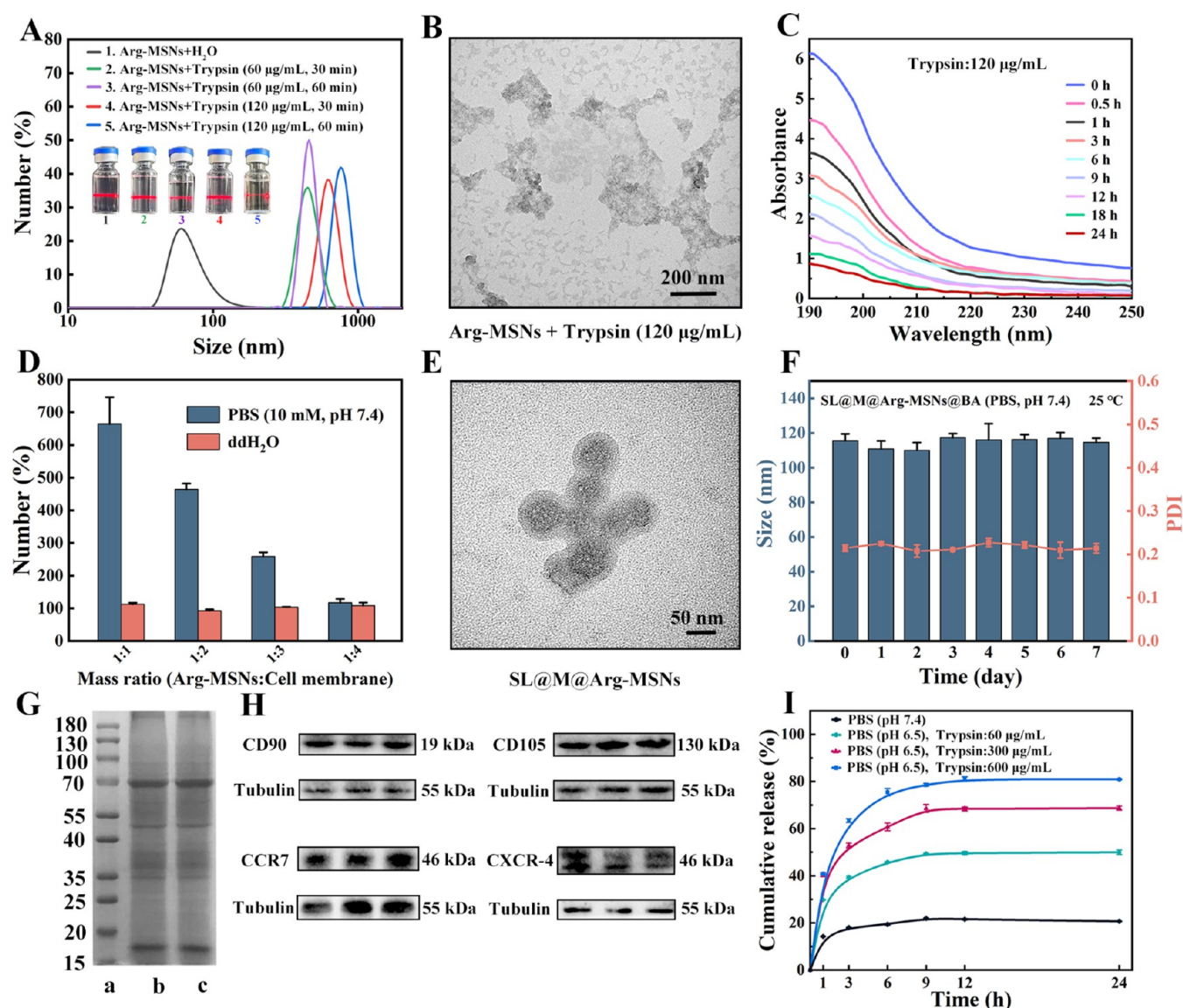


**Figure 2.** Trypsin-responsiveness of Arg-MSNs@BA and characterization of SL@M@Arg-MSNs@BA. (A) The particle size distribution and “Tyndall” light path diagram of Arg-MSNs cultured with trypsin-containing PBS medium (10 mM, pH 6.5) (trypsin concentration: 60 or 120 µg·mL<sup>-1</sup>). (B) Typical TEM images of Arg-MSNs after being incubated in the trypsin (120 µg·mL<sup>-1</sup>)-containing PBS medium for 30 min. (C) The UV-vis spectra of resuspended hydrolysates of Arg-MSNs after being incubated in the trypsin (120 µg·mL<sup>-1</sup>)-containing PBS medium for different times. (D) The particle size of M@Arg-MSNs@BA after being cultured in water and PBS medium at different mass ratios of Arg-MSNs to the BMSC membrane for 6 h. Data are mean ± standard error of the mean (SEM), *n* = 3. (E) Typical TEM images of M@Arg-MSNs. (F) The stability of SL@M@Arg-MSNs incubated under simulated physiological PBS conditions (10 mM, pH 7.4). (G) Sodium dodecyl sulfate-polyacrylamide gel electrophoresis (SDS-PAGE) for protein analysis and (H) the characteristic membrane protein expression evaluation. Line a, BMSC lysate; Line b, cell membrane fragments; Line c, membrane-coated NPs. (I) Drug-release curves of RhoB from M@Arg-MSNs cultured in PBS and trypsin (60, 300, and 600 µg·mL<sup>-1</sup>)-containing PBS medium. Data are mean ± SEM, *n* = 3.

were not visible in blank Arg-MSNs, indicating that the drug was successfully loaded into the NPs (Figure 1J). The drug encapsulation did not significantly affect the particle size distribution, with size and PDI remaining at ~68.8 nm and 0.194, respectively (Figure 1A). Even after 7 days of storage at room temperature, there was no alteration in particle size distribution or drug leakage (Figure S8).

We investigated the degradation behavior of Arg-MSNs in phosphate-buffered saline (PBS) media containing trypsin, which mimicked intracellular excessive trypsin conditions in the injured PAC microenvironment. After being incubated for 30 min in 60 µg·mL<sup>-1</sup> trypsin-containing mediums, DLS analysis revealed an increase in the particle size to the micron

level (Figure 2A). After 30 min of incubation Arg-MSN dispersion with 120 µg·mL<sup>-1</sup> trypsin, the “Tyndall path” of suspension rapidly diminished, with moving solid particles in the light path, while there were many solid precipitations at the bottom of the bottle after 60 min. TEM results revealed surface collapse of a certain portion of particles at 60 µg·mL<sup>-1</sup> trypsin, with debris aggregation at 30 min (Figure S9), while they even demonstrated bulk erosion of most of the particles at 120 µg·mL<sup>-1</sup> trypsin, indicating rapid degradation of Arg-MSNs into irregular fragments of the organosilica matrix (Figure 2B). The observed particulate aggregate and morphological changes can be attributed to the trypsin-catalyzed hydrolysis of the Arg-based amide bond bridge, which results in pronounced

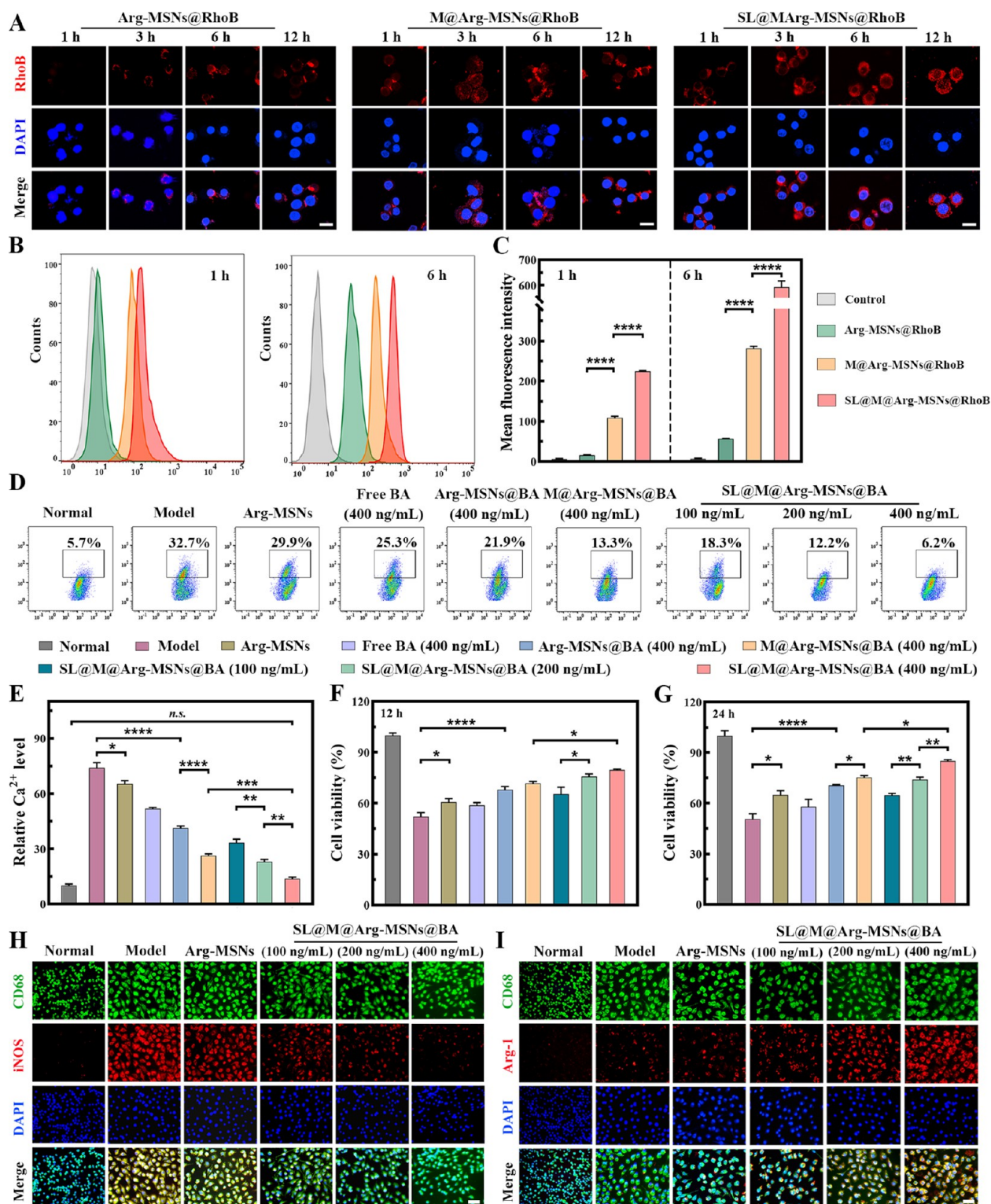


**Figure 3.** Cellular uptake and cell protective effects of SL@M@Arg-MSNs@BA in injured PACs. (A) Representative fluorescence microscopy images of cellular uptake of Arg-MSNs@RhoB, M@Arg-MSNs@RhoB, and SL@M@Arg-MSNs@RhoB in injured AR42J cells. Scale bar: 20  $\mu$ m. (B) Representative flow cytometry results and (C) quantitative flow cytometry results of the cellular uptake results of different RhoB-loaded NPs in injured AR42J cells. Data are mean  $\pm$  SEM,  $n = 3$ . (D) Flow cytometry analysis, and (E) quantitative flow cytometry results of intracellular  $Ca^{2+}$  levels in injured AR42J cells after 12 h of treatment with different formulations. The relative  $Ca^{2+}$  levels were calculated based on the mean fluorescence intensity in different cells assessed by flow cytometry. Data are mean  $\pm$  SEM,  $n = 3$ . The cell viability of acutely injured AR42J cells treated with different formulations for (F) 12 h and (G) 24 h. Data are mean  $\pm$  SEM,  $n = 5$ . (H) Representative images of immunofluorescence analysis of macrophage polarization phenotype-related CD68 (pan-macrophage marker) and iNOS (M1-macrophage marker) expression in RAW264.7 cells. Scale bar: 50  $\mu$ m.  $n = 5$ . (I) Representative images of immunofluorescence analysis of macrophage polarization phenotype-related CD68 (pan-macrophage marker) and Arg-1 (M2-macrophage marker) expression in RAW264.7 cells. Scale bar: 50  $\mu$ m.  $n = 5$ .

mechanical deformability and structural collapse of the framework, as well as the formation of silica fragments, which facilitate the aggregation of oligomers that have not yet fully degraded after 60 min of reaction. As degradation progressed, we found that the oligomers at the bottom were reduced after 2 h of incubation and even almost disappeared after 12 h of incubation in PBS containing trypsin (Figure S10). These oligomers were responsively degraded into small molecules possibly due to the substantial breakdown of the Arg-based organic bridge and the degradation step, where the silicon–oxygen bond structure further dissolves into silicic acid. In a simulated pathological PBS medium (10 mM, pH 6.5) supplemented with 60 or 120  $\mu\text{g}\cdot\text{mL}^{-1}$  trypsin, the absorption peak of Arg in Arg-MSNs decreased significantly over time, indicating substantial breakdown of the Arg-based organic bridge (Figures 2C and S11). These findings provide solid evidence that the skeletons of Arg-MSNs incorporating Arg-based amide bond bridges are susceptible to trypsin hydrolysis.

**Preparation and Characterization of Membrane-Camouflaged Arg-MSNs.** BMSC membrane fragments were surface-coated onto the Arg-MSNs@BA core using an ultrasonic bath to produce biomimetic M@Arg-MSNs@BA NPs, which were then modified with a lipophilic DSPE-PEG-SLIGRL (SL) targeting moiety (Figure S12), yielding SL@M@Arg-MSNs@BA NPs. The membrane coating varied the mass ratio of the Arg-MSN core to total membrane protein; at a 1:4 Arg-MSNs to protein weight ratio, the coverage was sufficient to prevent aggregation of NPs and maintain particle size and monodispersity in physiological PBS environments (Figure 2D). TEM results revealed that the BMSC membrane formed a dense and electron-transparent layer with visible integrity and consistency on the surface of the Arg-MSNs core, resembling a corona (Figure 2E). After membrane coating and targeted peptide surface modification, the hydrodynamic diameters of M@Arg-MSNs@BA and SL@M@Arg-MSNs@BA were slightly increased to  $\sim 116.9$  and  $\sim 125.7$  nm, respectively, but they both had a uniform size distribution (PDI: 0.197 and 0.199) (Figure 1A). After functionalizing the cell membrane, the surface charge of M@Arg-MSNs@BA was shifted to negative ( $\zeta$ -potential: from +29.8 to  $-32.3$  mV), resembling that of BMSC membrane-derived vesicles (Figure 1B). After inserting the SL targeting component, the  $\zeta$ -potential value changed to  $-23.9$  mV, attributed to the shielding effects of DSPE-PEG on negative charges as well as the weak positive charge of SLIGRL peptides on the NP surface. Encouragingly, the membrane-camouflaged NPs retained their particle size and monodispersity in physiological PBS conditions (10 mM, pH 7.4) for more than 7 days, suggesting good colloidal stability for further *in vivo* applications (Figure 2F).

As depicted in Figure 2G, the protein abundance analysis revealed that all membrane proteins were completely conserved on the NPs, preserving the characteristics of the source BMSC membranes. Western blots also confirmed the presence of typical BMSC-positive markers such as CD90, CD105, and CCR7 in both the extracted BMSC membranes and the membrane-coated formulation (Figure 2H). These markers were accompanied by the upregulation of the chemokine receptor CXCR4, which is responsible for homing to injured endothelial cells. These findings indicate that biomimetic membrane-camouflaged NPs successfully inherit

membrane proteins from parent BMSCs and may efficiently target the pancreatic inflammatory endothelium.

In simulated physiological PBS conditions (10 mM, pH 7.4), M@Arg-MSNs@RhoB released drugs at a significantly slower pace, with less than 14.2% drug leakage (alternative rhodamine B, RhoB) observed during the initial 1 h and 21.5% of the cumulative drug-release amount at 24 h (Figure 2I). Interestingly, the drug-release rate was higher in the mimic pathological microenvironment (PBS medium containing 60, 300, and 600  $\mu\text{g}\cdot\text{mL}^{-1}$  trypsin), achieving almost  $\sim 29.8$ , 40.5, and 40.8% cumulative drug release within the initial 1 h, respectively. Subsequently, the release profile leveled off at 6 h and reached a plateau at 24 h, with approximately 49.9, 68.7, and 80.9% of RhoB released from the NPs over a 24-h period. These results were consistent with the degradation behavior of Arg-MSNs, implying a framework degradation-mediated release mechanism.

#### Cytoprotective Effects on Pancreatic Acinar Cells.

Figure S13 shows that there were negligible changes in cell viability within the concentration range from 1 to 100  $\mu\text{g}\cdot\text{mL}^{-1}$  of NPs following a 24-h incubation, indicating excellent biocompatibility. The specific cell internalization of the as-prepared formulation was investigated in the injured PACs *in vitro*. As shown in Figures 3A and S14, the strong red RhoB fluorescence signal suggested that SL@M@Arg-MSNs@RhoB were much more intracellularly localized in PACs after a short period of incubation (1 h), with 11.6-fold and 2.4-fold average fluorescence intensity compared to Arg-MSNs@RhoB and M@Arg-MSNs@RhoB, respectively. Cell internalization of SL@M@Arg-MSNs@RhoB continuously increased throughout time and peaked at 6 h, which was nearly 2.6 times that of Arg-MSNs@RhoB. Flow cytometry data also demonstrated that SL@M@Arg-MSNs@RhoB had an apparent higher cellular uptake in PACs in the initial 1 h, with 14.5-fold and 2.0-fold increases in mean fluorescence intensity (MFI) compared to Arg-MSNs@RhoB and M@Arg-MSNs@RhoB, respectively, while exhibiting 10.5-fold and 2.1-fold at 6 h, respectively (Figures 3B,C, and S15). These results indicated that the SL@M@Arg-MSNs@RhoB were rapidly and effectively taken up by cells, which was most likely attributed to membrane-mediated internalization and specific binding of the SL peptide to the PAR2 receptor on PACs.

We further explored the scavenging effects of the as-prepared formulations on excessive cytosolic calcium levels ( $[\text{Ca}^{2+}]_i$ ), a critical upstream trigger for cell injury and necrosis, in tauro lithocholic acid 3-sulfate (TLCS)-induced injured PACs. At 12 h, TLCS elicited a significant increase in  $[\text{Ca}^{2+}]_i$ , which was approximately 7.4-fold higher than the baseline level (Figure 3D,E). The free BA drug and Arg-MSNs@BA at a BA dose of 400  $\text{ng}\cdot\text{mL}^{-1}$  lowered the peak level of  $[\text{Ca}^{2+}]_i$  by approximately 30.0 and 44.1%, respectively. The M@Arg-MSNs@BA-treated group (BA: 400  $\text{ng}\cdot\text{mL}^{-1}$ ) showed a stronger inhibitory effect (reduced by 64.3%), possibly because membrane coating improved colloidal stability, impeded drug leakage, enhanced cellular uptake efficiency, etc. Surprisingly, SL@M@Arg-MSNs@BA treatment reduced  $[\text{Ca}^{2+}]_i$  by 54.7%, even at a low BA dose (100  $\text{ng}\cdot\text{mL}^{-1}$ ). Notably, increasing the BA dosage in SL@M@Arg-MSNs@BA treatment led to a progressive and rapid decrease in  $[\text{Ca}^{2+}]_i$ . At a high dose of 400  $\text{ng}\cdot\text{mL}^{-1}$ , the suppression was approximately 81.3%, and the level nearly returned to its initial resting levels. These data clearly clarify that biomimetic

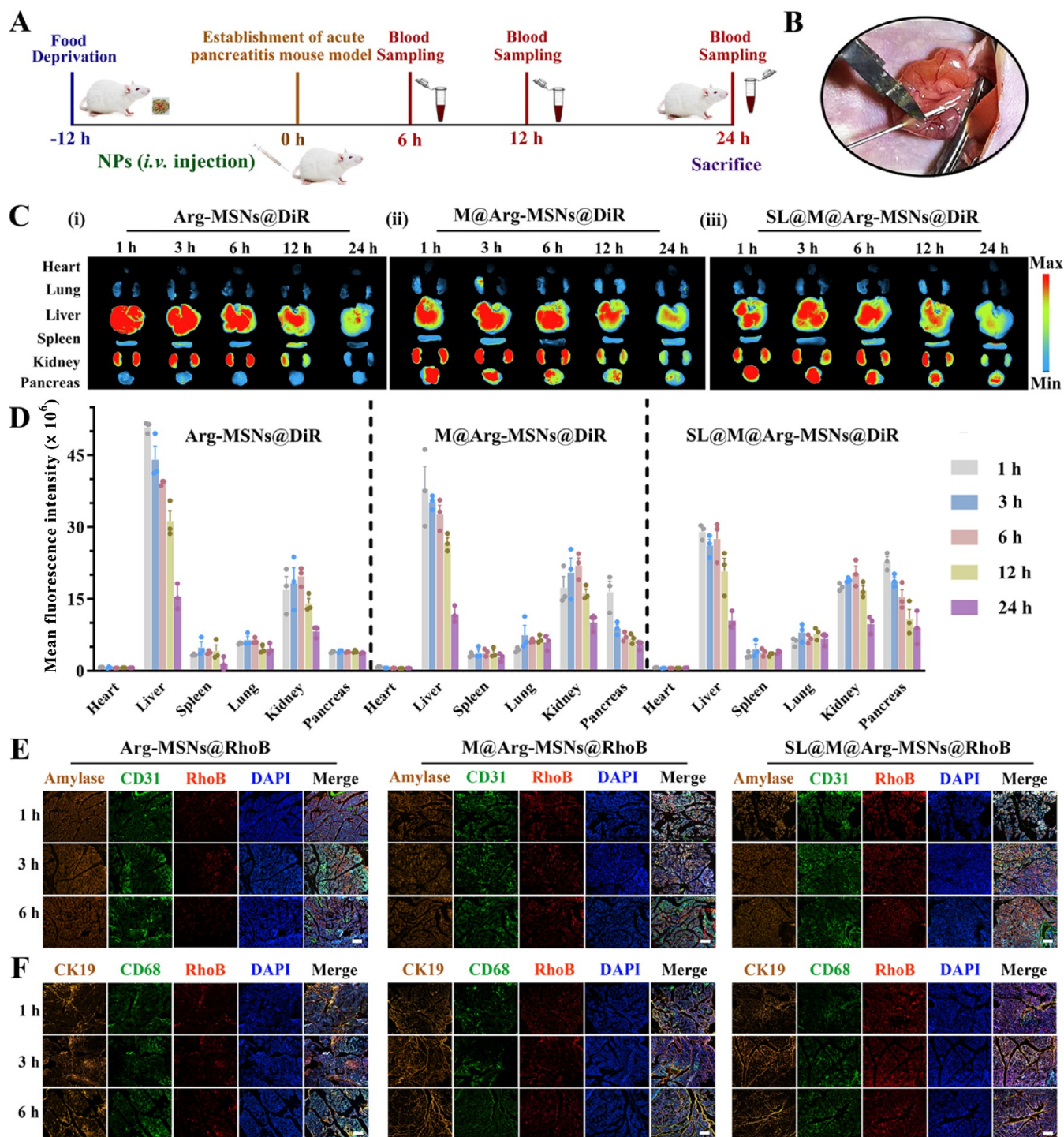


**Figure 4.** *In vivo* biodistribution and PAC targetability of SL@M@Arg-MSNs@DiR. (A) Experimental flowchart of the treatment procedures. (B) Representative photos of the model-establishing process. (C) The representative *ex vivo* fluorescence distribution images of major organs at different time points (1, 3, 6, 12, and 24 h) in AP mice treated with Arg-MSNs@DiR, M@Arg-MSNs@DiR, and SL@M@Arg-MSNs@DiR.  $n = 3$ . (D) Semiquantitative analysis of the relative fluorescence intensity of major organs after incubation with different formulations at varying times. Data are mean  $\pm$  SEM,  $n = 3$ . (E) The colocalization of RhoB-loaded NPs (red) in amylase-positive PACs (brownish yellow) and CD31-positive endothelial cells (green). Scale bar: 100  $\mu\text{m}$ . (F) The colocalization of RhoB-loaded NPs (red) in CD68-marked macrophages (green) and CK19-marked pancreatic ductal epithelial cells (brownish yellow). Scale bar: 100  $\mu\text{m}$ .

formulation protect PACs from TLCS-induced cytotoxic calcium overload in a BA dose-dependent manner.

As shown in Figure 3F,G, the blank Arg-MSN treatment provided moderate protection against cell injury and increased the cell viability from  $\sim 50.0\%$  to 60.6 and 64.9% at 12 and 24 h, respectively, implying that the therapeutic effect could be

attributed to the competitive consumption of trypsin by the enzyme-responsive skeleton structure, thereby preventing PAC autodigestion to some extent. The Arg-MSNs@BA (400  $\text{ng mL}^{-1}$ ) treatment restored cell viability to 68.0 and 70.6% at 12 and 24 h, respectively, whereas the M@Arg-MSNs@BA at the same dosage was significantly more effective in rescuing the

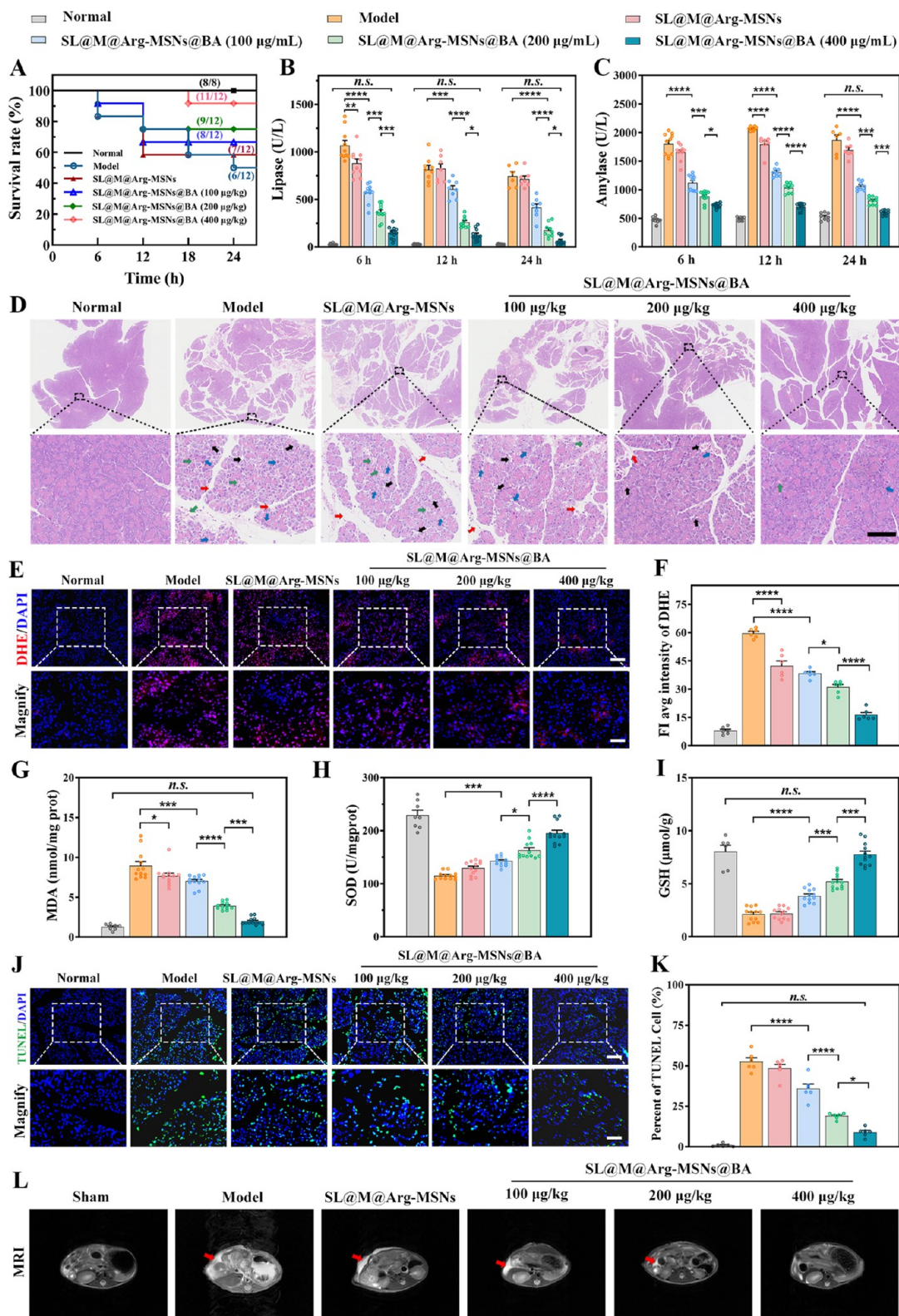


Figure 5. SL@M@Arg-MSNs@BA inhibits acinar cell death and restores pancreatic function. (A) Survival rate of AP mice after different treatments.  $n = 6-12$ . The serum (B) lipase and (C) amylase levels. Data are mean  $\pm$  SEM,  $n = 6-12$ . (D) H&E staining of the pancreas. The red arrow indicates lobular space widening, the black arrow indicates vacuolization of acinar cells, the green arrow indicates bleeding, and the blue arrow indicates infiltration of inflammatory cells. Scale bar: 100  $\mu$ m; (E) Representative images of DHE staining of pancreatic tissue, and (F) the semiquantitative results of its average fluorescence intensity. Scale bar: merge, 100  $\mu$ m; magnify, 50  $\mu$ m.  $n = 5$ . The (G) MDA, (H) SOD, and (I) GSH levels in the tissue homogenate. Data are mean  $\pm$  SEM,  $n = 12$ . (J) Representative images of TUNEL staining of pancreatic tissue, and (K) the semiquantitative results of its average apoptosis cell proportion. Scale bar: merge, 100  $\mu$ m; magnify, 50  $\mu$ m. Data are mean  $\pm$  SEM,  $n = 5$ . (L) Abdominal magnetic resonance imaging (MRI) of AP mice. The area marked by the red arrows represents the ascites part shown in the MRI scan.  $n = 3$ .

PACs, with viability reaching 71.7 and 75.3%, respectively. The SL@M@Arg-MSNs@BA formulation restored cell viability to 75.7 and 75.9% at a moderate dose (200 ng·mL<sup>-1</sup>), and almost 79.7 and 85.1% at a higher BA dose (400 ng·mL<sup>-1</sup>), suggesting a potent inhibitory effect against PAC injury in a BA dose-dependent manner.

As illustrated in Figures 3H and S16, the fluorescence signal of the M1-type macrophage marker iNOS obviously increased by 21.5-fold after being induced by the damaged PAC-conditioned medium in the model group. Treatment with free BA at a BA concentration of 400 ng·mL<sup>-1</sup> and blank Arg-MSNs slightly alleviated M1-phenotype polarization by 22.5 and 11.5%, respectively, as evidenced by a decrease in the proportion of red iNOS-positive cells. Compared to the Arg-MSNs@BA treatment groups, M@Arg-MSNs@BA and SL@M@Arg-MSNs@BA at a BA dosage of 400 ng·mL<sup>-1</sup> exhibited superior inhibitory effects on M1-polarization at the same dosage (400 ng·mL<sup>-1</sup>) as measured by a substantial reduction in the proportion of iNOS-positive cells (49.1 and 76.3% reduction, respectively). Additionally, SL@M@Arg-MSNs@BA (BA: 400 ng·mL<sup>-1</sup>) treatment shifted M0 macrophages to the anti-inflammatory M2-phenotype, with an 8.5-fold increase in MFI of M2-type macrophage marker Arg-1 compared to the model group (Figures 3I and S17). This was due to the fact that SL@M@Arg-MSNs@BA resulted in an 85.1% increase in cell viability restoration in PACs, which in turn led to a decrease in the release of damage-associated molecular patterns (DAMPs). Consequently, this partially reduced the transformation of inflammatory cells into proinflammatory M1-type macrophage and remodeled the macrophage to anti-inflammatory M2-type macrophage.

The formulation could be efficiently internalized by damaged PACs via SL ligand-mediated strong binding to the PAR2 receptor in the PACs' membrane, followed by membrane fusion-mediated cell uptake. Subsequently, the intracellular overloaded Ca<sup>2+</sup> is promptly eliminated in a BA dose-dependent manner. Additionally, the competitive consumption of trypsin is expedited via the Arg-based amide bridge in the MSNs. This mechanism effectively hinders the severe inflammatory response and protects cells from necrosis upstream in the PAC injury cascade.

**Targeting Efficiency of Biomimetic NPs toward Injured Acinar Cells in AP Mice.** This formulation showed low hemolysis *in vitro*, with a threshold rate of less than 5% at varied dosages (from 2 to 80 μg·mL<sup>-1</sup>), indicating acceptable hemocompatibility prior to dosage in AP mice induced by retrograde biliopancreatic duct injection of TLCS (Figure S18). Figure 4A,B depict a treatment schedule and a snapshot of the modeling process, respectively. As depicted in Figure 4C,D, DiR-loaded M@Arg-MSNs and SL@M@Arg-MSNs accumulated preferentially (a profound pancreatic fluorescence signal) in pancreatic tissues 1 h after intravenous injection (*i.v.*) in AP mice, with fluorescence intensity approximately 4.1 and 5.7 times higher than DiR-loaded Arg-MSNs, respectively. However, the accumulation of M@Arg-MSNs in the pancreas dropped at 3, 6, and 12 h after a single injection, but their fluorescence intensities remained 2.1, 1.8, and 1.6 times higher than Arg-MSNs, respectively; after 24 h, there was no visible fluorescence signal in the pancreas. Encouragingly, the SL@M@Arg-MSNs maintained localization and retention in the pancreas throughout time, with fluorescence intensities 4.5, 3.9, and 2.7 times higher than those of the Arg-MSNs group at 3, 6, and 12 h, respectively. Even after 24 h, a robust

fluorescence signal was still present in the pancreas, 2.4 and 1.6 times higher than that in the groups treated with Arg-MSNs and M@Arg-MSNs, respectively.

We then utilized immunofluorescence staining to visualize the selective targetability of formulation toward various cell types as well as particle homing patterns in different pancreatic cells such as acinar cells (amylase-positive cells), endothelial cells (CD31-positive cells), pancreatic ductal cells (CK19-positive cells), and macrophages (CD68-positive cells). Pearson's correlation coefficient (PCC) was calculated to assess the degree of colocalization between different fluorescent regions, with values closer to 1 indicating a stronger correlation. At 1 and 3 h after injection, the majority of RhoB-loaded M@Arg-MSNs (PCCs between RhoB with CD31 were ~0.701 and ~0.789, respectively) and RhoB-loaded SL@M@Arg-MSNs fluorescence (PCCs between RhoB with CD31 were ~0.690 and ~0.501, respectively) overlapped with CD31-positive cells (endothelial cells), while RhoB-loaded Arg-MSNs colocalized with only a few cells (PCCs between RhoB with CD31 were ~0.155 and ~0.186, respectively), signifying membrane-camouflaged NPs were recruited, localized, and retained within the injured endothelium region (Figures 4E and S19). Notably, the colocalization of SL@M@Arg-MSNs with the endothelium gradually decreased after 3 h; however, there was a more pronounced overlap with amylase-positive cells (PCC between RhoB with amylase was ~0.812) at 6 h postinjection compared to both the M@Arg-MSNs and the Arg-MSN-treated group. This finding indicates that SLIGRL peptide-modified NPs precisely and specifically target acinar cells following membrane-mediated endothelium recruitment and transvascular endothelial migration.

Figures 4F and S20 demonstrate a large overlap in fluorescence between RhoB-loaded Arg-MSNs and CD68-positive macrophages (PCCs between RhoB with CD68 were ~0.692 and ~0.582, respectively) at 1 and 3 h, indicating that the particles were substantially engulfed and internalized by the macrophages. The majority of these particles continued to overlap with macrophages throughout. Encouragingly, biomimetic membrane-coated NPs did not colocalize with CD68-positive macrophages at any time point (PCCs between RhoB with CD68 were <0.2 at 1, 3, and 6 h). After 6 h, only a small proportion of RhoB-loaded SL@M@Arg-MSNs colocalized with CK19-positive ductal cells (PCC between RhoB with CK19 was ~0.391).

Overall, these results suggest that BMSC membrane wrapping enables the evasion of unfavorable macrophage phagocytosis while also facilitating rapid and efficient recruitment and migration across the injured endothelium to the pancreas. Alternatively, the SLIGRL peptide promotes the precision and specificity of targeting while ensuring persistent retention in acinar cells, potentially curing injured acinar cells during AP.

**Pharmacodynamic Study of Biomimetic NPs in an AP Mouse Model.** As shown in Figure 5A, treatment with SL@M@Arg-MSNs@BA dramatically reduced the TLCS-induced high mortality rate in a dose-dependent manner (BA dosage: from 100 to 400 μg·kg<sup>-1</sup>). It is particularly noteworthy that a single dose of SL@M@Arg-MSNs@BA (BA: 400 μg·kg<sup>-1</sup>) significantly elevated the survival rate in AP mice from 50.0 to 91.6%. Notably, previous experiments revealed that further increasing the BA dose did not achieve ideal rescue of the pancreatic injury, with no additional improvement in the

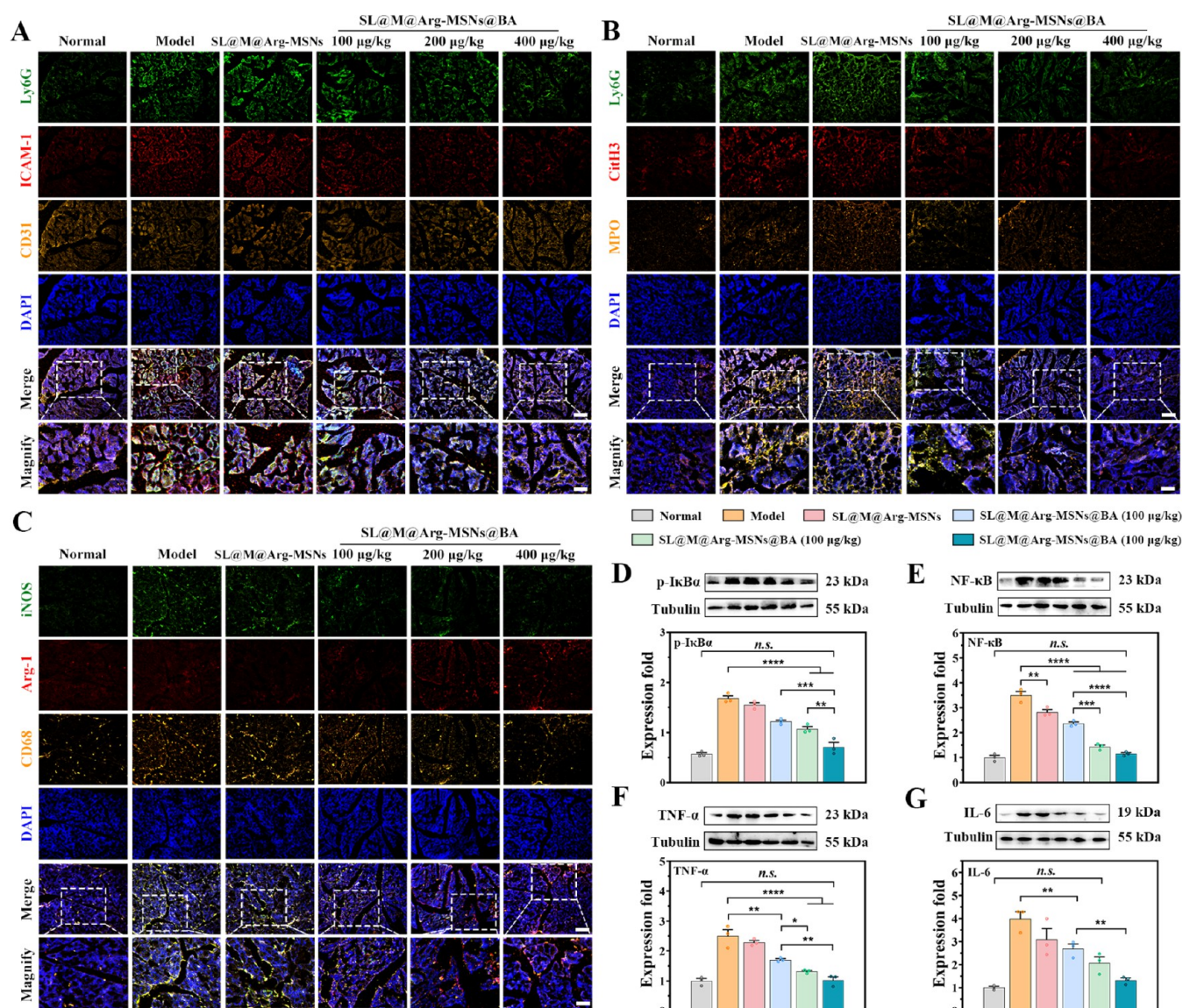


**Figure 6.** SL@M@Arg-MSNs@BA reduces recruitment of mononuclear macrophages and neutrophils, inhibits the release of neutrophil extracellular traps, and promotes M2-macrophage polarization. (A) Representative images of immunofluorescence staining of endothelial cells (CD31, brownish yellow), intercellular cell adhesion molecule-1 (ICAM-1, red), and neutrophils (Ly6G, green). (B) Representative images of immunofluorescence staining of neutrophils (Ly6G, green), citrulline histone H3 (CitH3, red), and myeloperoxidase (MPO, brownish yellow). (C) Representative images of immunofluorescence staining of total neutrophils (CD68, brownish yellow), M2 macrophages (Arg-1, red), and M1 macrophages (iNOS, green). Scale bar: merge, 100  $\mu\text{m}$ ; magnify, 50  $\mu\text{m}$ .  $n = 5$ . Western blot analysis of (D) p-I $\kappa$ B $\alpha$ , (E) NF- $\kappa$ B, (F) TNF- $\alpha$ , and (G) IL-6 expression and their quantification of protein expression in the corresponding pancreas.  $n = 3$ . Data are shown as mean  $\pm$  SEM.

survival rate (data not shown), indicating that there appears to be an optimal therapeutic dosage range of BA for AP treatment. The pancreas anatomy images revealed a significant alleviation in visible swelling and tissue collapse, as well as a restoration of tissue edges to sharpness in AP mice following SL@M@Arg-MSNs@BA dosage, whereas SL@M@Arg-MSNs only slightly restored the pancreatic morphology (Figure S21).

The typical diagnostic biomarkers of AP, lipase and amylase levels, were found to be elevated promptly and dramatically by 36.0 and 3.8 times, respectively, in mice following the TCLS insult at the first 6 h and maintained a high level at 24 h (Figure 5B,C). After 6 h of treatment with blank SL@M@Arg-MSNs, serum lipase was reduced by 17.5%; while amylase levels reduced by 13.2% at 12 h. This therapeutic effect could be explained by the degradation of the Arg-MSNs backbone,

which leads to the competitive consumption of excess activated trypsin, whereas the binding of the SL peptide (serving as a receptor agonist) to the PAR2 receptor could potentially reduce pancreatitis severity.<sup>43</sup> A single low dose of SL@M@Arg-MSNs@BA (BA: 100  $\mu\text{g}\cdot\text{kg}^{-1}$ ) successfully lowered lipase levels by 46.4, 25.1, and 44.3%, and amylase levels by 37.7, 36.9, and 43.1% at 6, 12, and 24 h, respectively. Increasing the BA dosage resulted in a consistent reduction in lipase and amylase levels throughout the treatment period. In SL@M@Arg-MSNs@BA-treated group (BA: 400  $\mu\text{g}\cdot\text{kg}^{-1}$ ), the lipase and amylase levels dropped by 85.9 and 59.6% at 6 h, respectively, and even returned to normal levels at 24 h. These results indicate that adopting the SL@M@Arg-MSNs@BA formulation might lead to a distinguished recovery of pancreatic functions in a BA dose-dependent manner.

In histopathological analysis, administration of SL@M@Arg-MSNs@BA at BA dosages of 100 and 200  $\mu\text{g}\cdot\text{kg}^{-1}$  exhibited less lobular space widening, reduced acinar necrosis and inflammatory cell infiltration, and moderate effects on pancreatic edema compared to severe histopathological injury in AP mice (Figure S4D). Fortunately, AP mice receiving SL@M@Arg-MSNs@BA (BA: 400  $\mu\text{g}\cdot\text{kg}^{-1}$ ) can restore the pancreas's anatomy and histopathology to a state nearly identical to that of healthy mice.

Encouragingly, compared to the AP model group, the group that received a single dosage of SL@M@Arg-MSNs@BA at 100  $\mu\text{g}\cdot\text{kg}^{-1}$  of BA exhibited significant inhibition of oxidative stress injury, as evidenced by a 35.8% reduction in superoxide value (DHE fluorescence intensity) (Figures S5E,F, and S22) and a 21.4% decrease in lipid peroxidation products MDA level (Figure S5G). As BA dosage increased from 100 to 400  $\mu\text{g}\cdot\text{kg}^{-1}$ , DHE and MDA levels decreased further. At a high dosage (BA: 400  $\mu\text{g}\cdot\text{kg}^{-1}$ ), DHE and MDA levels were drastically reduced by 72.5 and 77.8%, respectively, with MDA levels comparable to the normal group. Even a single low dosage of SL@M@Arg-MSNs@BA (BA: 100  $\mu\text{g}\cdot\text{kg}^{-1}$ ) restored oxidative GSH and SOD activity by 1.8 and 1.2 times, respectively (Figure S5H,I). Increasing the BA dosage to 400  $\mu\text{g}\cdot\text{kg}^{-1}$  led to a 3.7-fold rise in GSH and a 1.7-fold restoration of SOD levels, returning them to normal levels compared to the model group. These results indicate that BA-loaded formulation treatment significantly improves cellular redox status in AP mice, potentially protecting critical cellular proteins or organs from the lethal effects of oxidative stress injury.

Figures S5J,K, and S23 reveal that TLCS induced massive TUNEL-positive apoptosis in the AP mice's pancreatic tissue ( $52.0 \pm 2.4\%$ ). SL@M@Arg-MSNs@BA treatment significantly reduced apoptotic cells in a dose-dependent manner compared to the model group, with  $35.9 \pm 6.5$ ,  $18.9 \pm 1.7$ , and  $8.9 \pm 2.6\%$  of TUNEL-positive cells at 100, 200, and 400  $\mu\text{g}\cdot\text{kg}^{-1}$  of BA dosage, respectively, while even returning to a level comparable to the normal group at a dose of 400  $\mu\text{g}\cdot\text{kg}^{-1}$ .

Pancreatitis-associated ascitic fluid is one of the most common serious complications of severe AP, with an incidence of more than 60%.<sup>44,45</sup> Patients with massive ascites generally experience elevated severity of the disease, a prolonged disease course, a worse prognosis, and a higher mortality rate than those without ascites.<sup>46</sup> In the model group, abdominal magnetic resonance imaging (MRI) scans revealed a significant accumulation of ascitic fluid (obvious watery fluid signal) in the peritoneal cavity, which could be attributed to impaired pancreatic microcirculation, increased vascular permeability, and fluid exudation from the intravascular space (Figure S5L). In contrast, the group that received a sham operation had minimal or no ascites. The administration of SL@M@Arg-MSNs@BA (400  $\mu\text{g}\cdot\text{kg}^{-1}$ ) greatly reduced the volume of ascitic fluid in the peritoneal cavity of mice, with no notable difference compared to the sham group. The treatment of SL@M@Arg-MSNs@BA at BA doses of 100 and 200  $\mu\text{g}\cdot\text{kg}^{-1}$  exhibited moderate effects on reducing ascites.

Furthermore, we surprisingly found that AP mice administered a signal dose of SL@M@Arg-MSNs@BA (BA: from 100 to 400  $\mu\text{g}\cdot\text{kg}^{-1}$ ) significantly inhibited the lung pathological changes, as evidenced by a restoration of alveolar wall thickness, almost no alveolar edema, and inflammatory cell infiltration, indicating that this formulation may potentially avert the occurrence of lung injury complications (Figure S24).

**Attenuation of the Systemic Inflammatory Cascade in All Stages of AP Mice.** The excessive inflammatory response cascade mediated by immune cells is one of the key factors in the pathogenesis of severe AP, with neutrophils being the initial cell type recruited to the injured pancreas. As shown in Figure 6A, we observed a significant increase in neutrophil recruitment around the injured endothelium, which was confirmed by the colocalization of the Ly6G-positive region (green fluorescence) with intercellular adhesion molecule-1 (ICAM-1, red fluorescence) and endothelia (CD31, brownish yellow fluorescence), indicating the initiation of proinflammatory signaling. The administration of SL@M@Arg-MSNs in AP mice resulted in a marginal inhibition of injured molecule ICAM-1 expression (reduced by 12.7%) in the inflamed endothelium (Figure S25A). Treatment with SL@M@Arg-MSNs@BA at a low BA dose (100  $\mu\text{g}\cdot\text{kg}^{-1}$ ) inhibited neutrophil invasion and migration in AP mice, resulting in lower expression of ICAM-1 (reduced by 35.9%) and Ly6G (reduced by 31.4%), and reduced the fluorescence colocalization of Ly6G/ICAM-1/CD31 (Figure S25B,C). It is encouraging that the group treated with a high dose of SL@M@Arg-MSNs@BA (400  $\mu\text{g}\cdot\text{kg}^{-1}$ ) exhibited significantly lower neutrophil infiltration at the injured endothelium in AP mice, with ICAM-1 and Ly6G levels reduced by 70.0 and 68.3%, respectively, while their fluorescence intensity of ICAM-1 was even visibly close to that of healthy mice.

We then found extensive formation of neutrophil extracellular traps (NETs) in the injured pancreatic tissue, as evidenced by massive myeloperoxidase (MPO, brownish yellow fluorescence) and citrullinated histone 3 (CitH3, red fluorescence) expression, both of which merged with Ly6G-positive regions (activated neutrophils) in the model group (Figures 6B and S26). This was directly related to the driving force of largely released chemokines, cytokines, and adhesion molecules from injured PACs.<sup>47</sup> The SL@M@Arg-MSNs@BA intervention in AP mice significantly reduced infiltrating neutrophils and NET formation in pancreatic tissue, as evidenced by a significant decrease in colocalized Ly6G/MPO/CitH3. Unexpectedly, the mice treated with a high dose of SL@M@Arg-MSNs@BA (BA: 400  $\mu\text{g}\cdot\text{kg}^{-1}$ ) showed less expression of MPO and CitH3, with their expression reduced by 84.8 and 81.5%, respectively (Figure S26A,B), and even a negligible Ly6G/MPO/CitH3 triple staining-positive area (Figure S26C), indicating a significant reduction in NETs in response to PAC injury.

We also discovered a significant increase in pan-macrophages (CD68, brownish yellow fluorescence) with a high number of proinflammatory M1-type macrophages (an obvious overlay of iNOS with CD68) responding to severe pancreas injury in the model group, validating macrophage recruitment and M1-type macrophage transformation in the injured pancreas microenvironment (Figure 6C). The administration of SL@M@Arg-MSNs@BA (BA: 100 and 200  $\mu\text{g}\cdot\text{kg}^{-1}$ ) blocked inflammatory-related macrophage recruitment with a significant reduction in CD68 fluorescence intensity by 14.9 and 26.5%, as well as reduced iNOS-positive M1-type by 29.4 and 70.3% (Figure S27A,B). Moreover, the treatment with SL@M@Arg-MSNs@BA at 100 and 200  $\mu\text{g}\cdot\text{kg}^{-1}$  of BA promoted the repolarization into anti-inflammatory Arg-1-positive M2-type by 4.3-fold and 9.8-fold, respectively (Figure S27C). A high dose of SL@M@Arg-MSNs@BA (BA: 400  $\mu\text{g}\cdot\text{kg}^{-1}$ ) treatment significantly reduced iNOS-positive M1-type by 88.8%, an almost upregulated Arg-1-positive M2-

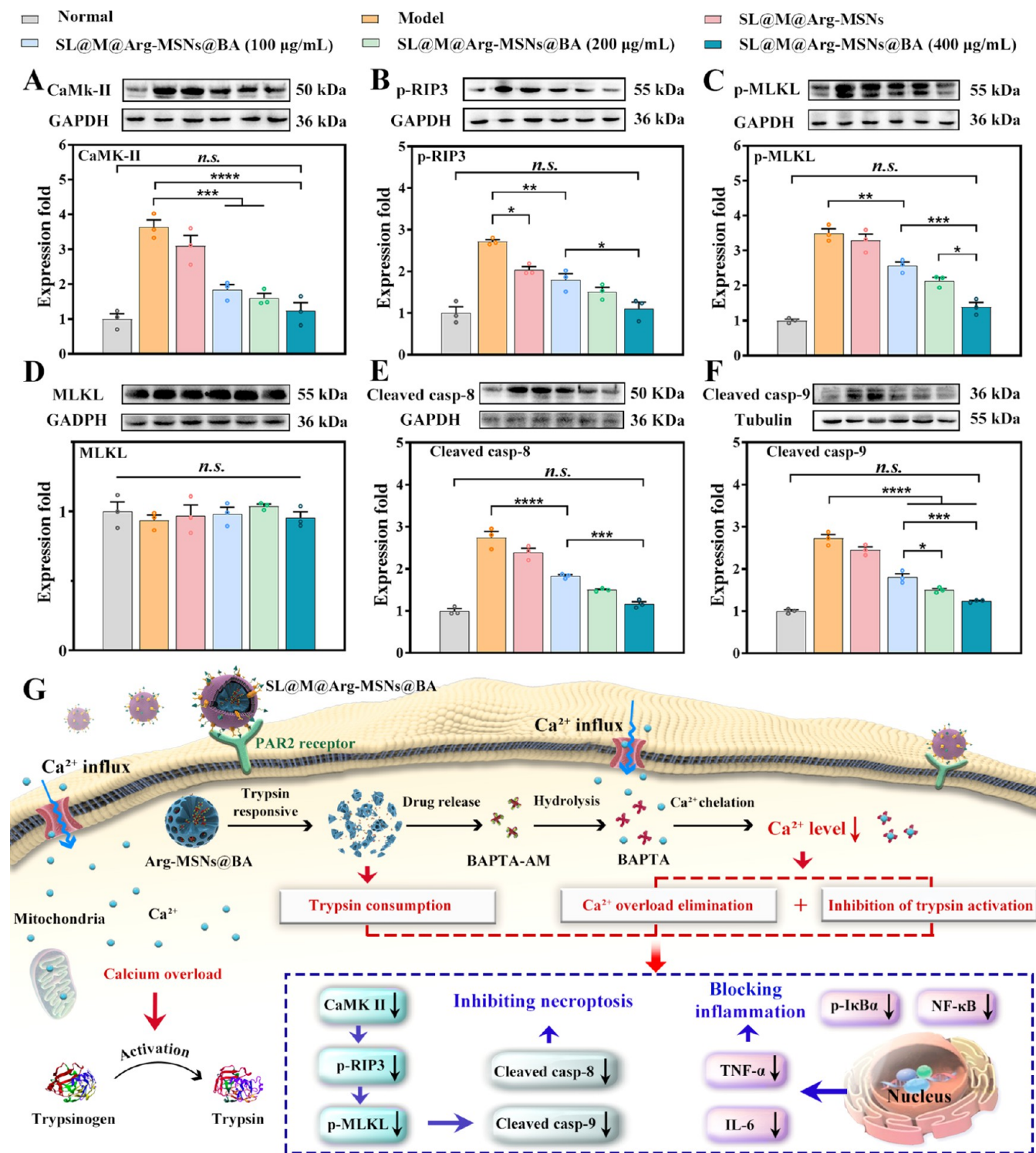


**Figure 7.** Treatment mechanism of SL@M@Arg-MSNs@BA in AP mice. The representative Western blot bands and semiquantitative results of (A) CaMK-II, (B) p-RIP3, (C) p-MLKL, (D) MLKL, (E) cleaved caspase 8, and (F) cleaved caspase 9. Data are shown as mean  $\pm$  SEM  $n = 3$ . (G) Illustration of the treatment mechanism of SL@M@Arg-MSNs@BA in PACs.

type by 13.1-fold, and an obvious fluorescence overlay of Arg-1/CD68 in the tissue of AP mice, which would help to suppress the secretion of detrimental inflammatory components and facilitate anti-inflammatory species in the pancreatic microenvironment.

In AP mice, protein expression levels of  $\text{I}\kappa\text{B}\alpha$  phosphorylation (p- $\text{I}\kappa\text{B}\alpha$ ) and nuclear NF- $\kappa\text{B}$ , a critical regulator of the inflammatory response, were elevated by 2.9- and 3.5-fold,

respectively (Figure 6D,E). SL@M@Arg-MSNs treatment reduced NF- $\kappa\text{B}$  p65 nuclear translocation by 19.3% compared to the model group, but did not affect  $\text{I}\kappa\text{B}\alpha$  phosphorylation. It is worth noting that the as-prepared SL@M@Arg-MSNs@BA at BA dosages of 100, 200, and 400  $\mu\text{g}\cdot\text{kg}^{-1}$  significantly reduced p- $\text{I}\kappa\text{B}\alpha$  expression by 27.5, 36.1, and 57.5%, respectively, and inhibited NF- $\kappa\text{B}$  p65 nuclear translocation by 32.5, 59.0, and 67.1%. At a dose of 400  $\mu\text{g}$ .

kg<sup>-1</sup>, both levels were lowered to near-normal levels. Furthermore, blocking the cellular inflammatory pathway impeded the secretion of detrimental proinflammatory cytokines in AP mice. The levels of TNF- $\alpha$  and IL-6 decreased by 31.7 and 32.4%, respectively, at a low dose of SL@M@Arg-MSNs@BA (BA: 100  $\mu\text{g}\cdot\text{kg}^{-1}$ ), and further reduced by 47.4 and 47.8% at the medium dose of SL@M@Arg-MSNs@BA (BA: 200  $\mu\text{g}\cdot\text{kg}^{-1}$ ), respectively (Figure 6F,G). The high-dose formulation almost lowered TNF- $\alpha$  and IL-6 expression by 58.9 and 66.7%, respectively, bringing it close to the normal group.

These findings clearly demonstrate that the as-prepared formulations can effectively inhibit endothelial damage, and subsequent immune cell migration (neutrophil and macrophage), reduce NET production, reprogram macrophages, and block massively proinflammatory mediator release in a BA dose-dependent manner. This is due to the BA-mediated inhibitory effects of injury progression in PACs via rapid chelation of overloaded Ca<sup>2+</sup>, which results in less PAC damage and substantially lower DAMP production. Furthermore, trypsin consumption by the Arg-MSN skeleton structure would limit trypsin autodigestion while simultaneously blocking tissue damage. Both eventually inhibit and regulate downstream local and systemic inflammatory responses, disrupt the inflammatory-amplified destructive cycle, protect peripancreatic tissue, and effectively reduce the risk of distal tissue damage.

**SL@M@Arg-MSNs@BA Blocked Canonical Necroptotic Signaling in AP Mice.** Severe AP has been associated with massive PAC necrosis, which leads to intense local pancreatic necroinflammation and may induce multiple organ dysfunction syndrome, ultimately augmenting the disease's mortality.

The administration of SL@M@Arg-MSNs@BA at 100, 200, and 400  $\mu\text{g}\cdot\text{kg}^{-1}$  lowered CaMK-II levels by 49.6, 55.9, and 66.1% in AP mice, respectively (Figure 7A). However, SL@M@Arg-MSNs showed no effect on inhibiting CaMK-II signaling activation. This also implies that efficient CaMK-II inhibition is closely related to BA-mediated Ca<sup>2+</sup> elimination, which may effectively inhibit the conduction of the involved downstream necroptotic signaling pathways.

Furthermore, downstream phosphorylation of RIP3 (p-RIP3) and MLKL (p-MLKL) was activated, as evidenced by significantly elevated levels of p-RIP3 (2.7-fold increase) and p-MLKL (3.5-fold increase) in AP mice compared to the normal group (Figure 7B,C). SL@M@Arg-MSNs@BA at BA dosages of 100, 200, and 400  $\mu\text{g}\cdot\text{kg}^{-1}$  significantly downregulated the expression of necrotic markers p-RIP3 and p-MLKL in the SL@M@Arg-MSNs@BA-treated group. It is worth noting that the administration of SL@M@Arg-MSNs@BA at a high dose (400  $\mu\text{g}\cdot\text{kg}^{-1}$ ) to AP mice resulted in much stronger inhibition of p-RIP3 (reduced 59.2%) and p-MLKL (reduced 60.2%) expression, with levels comparable to the normal group. Throughout the treatment period, the expression of control total MLKL proteins remained unchanged in each group (Figure 7D). Furthermore, this formulation at 100 and 200  $\mu\text{g}\cdot\text{kg}^{-1}$  doses of BA has effective inhibitory effects on downstream cleaved caspase 8 expression with reduced levels by 45.3 and 33.3%, respectively (Figure 7E), while also inhibiting cleaved caspase 9 with reductions of 33.7 and 44.9%, respectively (Figure 7F). At a high dose of BA (400  $\mu\text{g}\cdot\text{kg}^{-1}$ ), the as-prepared formulation almost completely inhibited necroptosis, reducing cleaved caspase 8 and cleaved

caspase 9 levels by 57.6 and 54.6%, respectively, and even reverting expression to normal levels.

The molecular-level results suggest that SL@M@Arg-MSNs@BA provides direct inhibition of acinar necrosis in early AP by inhibiting the necroptotic signaling pathway involving CaMK-II/p-RIP3/p-MLKL (Figure 7G). The treatment decreased the formation of active MLKL complexes in the plasma membrane and prevented the release of DAMPs, resulting in decreased cell swelling, membrane rupture, and inflammatory responses. Additionally, the formulation also blocked the activation of caspase 8 and caspase 9 in necroptotic cascade signaling. One possible explanation for this inhibitory effect, which is dose-dependent, is that the BA drug rapidly chelates intracellularly overloaded calcium and regulates the balance of Ca<sup>2+</sup> in PACs to restore healthy cellular status. The results provide a molecular-level explanation for the formulation's ability to halt disease progression and reinstate pancreatic function in mice with acute pancreatitis.

**Safety Evaluation.** Blood biochemistry markers such as alanine aminotransferase (ALT) and aspartate aminotransferase (AST), blood urea nitrogen (BUN), and creatinine (Cre) indicated no significant changes among the groups compared to the control group (Figure S28A–D). Besides, H&E staining revealed no histological changes in major organs such as the heart, liver, spleen, and kidneys in AP mice treated with different formulations (Figure S29). These findings indicated that the dosage of the as-prepared formulation had no notable toxicity in the AP mice, suggesting a high level of biocompatibility. Notably, the degradation and metabolism of silica NPs are still significant issues due to their potential long-term and latent pathogenic effects on physiological systems. Nonetheless, our as-prepared trypsin-responsive Arg-MSNs sensitively respond to excess trypsin in injured PACs to accelerate particle degradation and rapidly break down into silica-based carboxylates or amino derivatives. Thereafter, the interaction between the remaining silicon–oxygen bond structure and the adsorbed water molecules will be accelerated to create multiple silanol groups, which further engage in ion exchange reactions to liberate nontoxic silicic acid.<sup>48,49</sup> Eventually, these silicic acids would be excreted through urine, thus providing robust assurance for biosafety *in vivo*.

## CONCLUSIONS

In summary, we presented the successful covalent embedding of trypsin-cleavable silica precursor containing Arg-based amide bonds into a silica framework, resulting in the construction of organo-bridged trypsin-responsive MSNs for matrix degradation-controlled drug delivery. After surface-coating with BMSC membrane and surface modification with the PAC targeting peptide, SL@M@Arg-MSNs@BA exhibited recruitment to the inflammatory microenvironment and precise targeting to injured PACs.

In the AP mouse model induced by TCLS, a single dose of SL@M@Arg-MSNs@BA localized rapidly in the injured pancreas, accumulating 5.7-fold and 4.5-fold more than Arg-MSNs after 1 and 3 h, respectively; after 12 h, sustained high-level accumulation (2.6-fold) was observed. The nanoparticles underwent self-immolation upon exposure to the hyperactive trypsin, resulting in the complete disintegration of the NPs' skeleton and subsequent release of the payload BA. This formulation mechanically inhibits the cell necroptosis pathway (CaMK-II/p-RIP3/p-MLKL/caspase-8,9) and blocks the

inflammatory cascade (p-I $\kappa$ B $\alpha$ /NF- $\kappa$ B/IL-6/TNF- $\alpha$ ) by rapidly and effectively eliminating overloaded Ca<sup>2+</sup> via released BA and by competitively consuming trypsin via NPs' skeleton, thereby rescuing the injured PACs upstream the cell death signaling pathway.

In AP mice, a single injection of this formulation (BA: 400  $\mu$ g·kg<sup>-1</sup>) significantly restored redox status by inhibiting the production of lipid peroxidation products (MDA: 77.8% reduction) and downregulating downstream superoxide levels (DHE: 72.5% reduction), while also restoring the antioxidative activities of GSH and SOD by 3.6 and 1.7 times, respectively. Concurrently, it effectively reduced the cell apoptosis ratio in damaged pancreatic tissue from 52  $\pm$  2.4 to 8.9  $\pm$  2.6%. SL@M@Arg-MSNs@BA restored pancreatic function and histopathology, whereas lipase and amylase levels dropped by 85.9 and 59.6% after 6 h, respectively, and returned to normal levels after 24 h. This formulation impeded the recruitment of circulating neutrophil cells and downstream endothelial damage (decreased CD31/ICAM-1/Ly6G colocalization fluorescence), inhibited the generation of NETs (Ly6G/CitH3/MPO), and reprogrammed the macrophage to an anti-inflammatory M2-type macrophage, eventually inhibiting the local and systemic inflammatory response. Therefore, SL@M@Arg-MSNs@BA exerted a comprehensive protective effect *in vivo*, not only preventing ascites and lung injury but also increasing the survival rate of AP mice from 50 to 91.6%.

This biomimetic trypsin-responsive nanocarrier quickly and specifically reverses PAC damage at the early stages of cell injury via ion homeostasis regulation and trypsin activity inhibition, thereby blocking the pathophysiological progress of AP, which has great clinical translation potential.

## MATERIALS AND METHODS

**Materials.** L-Arginine, succinic anhydride, N-methylmorpholine (NMM), isopropyl chloroformate (IPCF), APTMS, TEAH<sub>3</sub>, and CTAB were purchased from Aladdin. DSPE-PEG<sub>2000</sub>-NHS was obtained from Leyan (Shanghai, China). The Fluo-4 AM fluorescent probe and BUN kits were purchased from Solarbio Science & Technology Co., Ltd. (Beijing, China). Cell culture flask and centrifuge tube obtained from SAINING Biotechnology. CCK8 (CP0001) was obtained from Shanghai Cytoch Biotechnology Co., Ltd. Protease inhibitor cocktail (SP002720001) and DMEM/high-glucose medium (SP032010500) purchased from Sperikon Life Science & Biotechnology Co., Ltd. 20 mm glass-bottom dishes were obtained from NEST Biotechnology Co. Ltd. (Wuxi, China). Amylase (G0511W) kits were purchased from Suzhou Grace Biotechnology Co., Ltd. Lipase, MDA, Cre, AST, and ALT kits were purchased from Jiancheng Co. Ltd. SOD and GSH kits were purchased from Beijing Boxbio Science & Technology Co., Ltd. TLCS was purchased from Sigma Aldrich. Rhodamine B (#A4705) and DiR (#B8806) were acquired from APEX BIO (Houston). The DHE probe, BCA, and TUNEL assay kits were purchased from KeyGEN Biotech Co., Ltd. (Nanjing, China). CD31-specific antibodies were purchased from R&D Systems. MPO (#ab300650), CitH3 (#ab281584), and CD68 (#ab53444)-specific antibodies were purchased from Abcam. Arg-1 (#CLS94-66129), ICAM-1 (#10020-1-AP),  $\alpha$ -amylase (#12540-1-AP), and CK19 (#10712-1-AP)-specific antibodies from Proteintech. iNOS (#HA722031) form HUABIO. Ly6G (#88876s)-specific antibody was purchased from Cell Signaling Technology, Inc. SDS-PAGE Gel Preparation Kit (#P2012) was purchased from New Cell & Molecular Biotech. p-NF- $\kappa$ B p65 (bs-3485R) was purchased from Bioss Co., Ltd. (Beijing, China). Fetal bovine serum,  $\beta$ -tubulin (#abs171597), TNF- $\alpha$  (#abs05092), and GAPDH (#abs830030)-specific antibodies were purchased from Absin Bioscience Inc. (Shanghai, China). IL-6 (WL02841), I $\kappa$ B $\alpha$  (WL01936), and p-I $\kappa$ B $\alpha$  (WL02495)-specific antibodies were

purchased from Wanleibio Inc. (Beijing, China). MLKL (YP-Ab-10482) and p-MLKL (#YP-Ab-14260)-specific antibodies were purchased from UpingBio Technology Co. Ltd.; Hangzhou, China.

**Synthesis and Characterization of Arg-Suc-AcOH.** The alkoxysilane derivatives of arginine were prepared by reacting arginine with APTMS in two steps, with succinic anhydride acting as a linker. First, L-arginine (1.0 equiv, 10.0 g, 57.4 mmol) and succinic anhydride (1.2 equiv, 6.9 g, 68.9 mmol) were added dropwise in acetic acid and stirred under a nitrogen gas atmosphere at 55 °C overnight. The white solid crude Arg-Suc product (Arg-Suc-AcOH) (9.6 g, 50.0% yield) was obtained by postprecipitation with diethyl ether, followed by the collection of the solids and drying under reduced pressure. <sup>1</sup>H NMR spectrum (600 MHz, deuterium oxide).  $\delta$  4.32 (dd,  $J$  = 9.0, 4.9 Hz, 1H), 3.14 (t,  $J$  = 6.9 Hz, 2H), 2.62–2.51 (m, 4H), 1.86 (m,  $J$  = 14.1, 9.4, 6.7, 5.0 Hz, 1H), 1.70 (m,  $J$  = 14.2, 9.4, 5.4 Hz, 1H), and 1.59 (m,  $J$  = 13.5, 9.6, 7.0 Hz, 2H).

**Synthesis and Characterization of Arg-Suc-APS.** Arg-Suc-AcOH (1.0 equiv, 1.2 g, 4.3 mmol), NMM (3.0 equiv, 1.2 mL, 12.9 mmol), and IPCF (3.0 equiv, 1.58 g, 12.9 mmol) toluene solutions were reacted in tetrahydrofuran under a nitrogen gas atmosphere for 2 h. Then, APTMS (3.0 equiv, 1.88 mL, 12.9 mmol) was added and stirred at 45 °C for another 18 h. After filtration and washing with tetrahydrofuran, the solid products were dissolved in methanol and filtered, concentrated under reduced pressure until completely dry, yielding Arg-Suc-APS as a yellowish solid (1.23 g, 57.4% yield). <sup>1</sup>H NMR spectrum (600 MHz, DMSO-*d*<sub>6</sub>).  $\delta$  4.16 (td,  $J$  = 8.6, 5.0 Hz, 1H), 3.80 (t,  $J$  = 5.0 Hz, 18H), 3.22–3.04 (m, 6H), 2.45–2.36 (m, 4H), 1.92–1.48 (m, 8H), 1.41–0.42 (m, 4H).

**Preparation of Arg-MSNs.** Arg-based amino acid-bridged MSNs were prepared via a modified sol-gel method using CTAB as the structure-directing agent, TEOS and Arg-Suc-APS with amino acid-bridged groups as co-silica sources. Briefly, CTAB (2.5 g) and TEAH<sub>3</sub> (0.11 mL) were dissolved in 50 mL of ultrapure water and stirred at 95 °C for 1 h. Subsequently, precursor TEOS (1.25 mL) was added, and the reaction was run for another hour. Then, a mixture of coprecursors of 1 mL methanol solution of Arg-Suc-APS (700 mg) and 0.96 mL of TEOS (with a molar ratio of 1:6) was added dropwise to surfactant solution and stirred at 95 °C for 3 h with a stirring speed of 1400 rpm. The reaction mixture was collected after being centrifuged for 15 min and washed thrice with water and ethanol alternately. Arg-MSNs were obtained by etching with ammonium nitrate (1.2 g) in an ethanol solution (62.5 mL) at 60 °C for 1 h, followed by three washes with ethanol and drying under vacuum.

**Characterization of Arg-MSNs.** The particle size and zeta potential of the formulation were characterized using a DLS spectrometer (Malvern Zetasizer Nano Instrument, ZEN3600, U.K.). The NPs' morphology was characterized by TEM (HT7700, Hitachi, Japan). Furthermore, the morphology and distribution of elements in NPs were analyzed by scanning electron microscopy (SEM) images and EDS mapping using a SEM instrument (SU8010, Hitachi, Japan). The specific surface area, the corresponding pore size distribution of Arg-MSNs were analyzed using a fully automated BET surface (volume) analyzer (NOVA2200e, Quantachrome). The UV-vis adsorption spectra of MSNs, Arg, and Arg-MSNs were recorded on a nanodrop instrument (Thermo). The chemical compositions of particles and structural features of the particles were analyzed by XPS (ESCALab250, Thermo) and XRD (Bruker D8 Focus;  $2\theta$  ranging from 5 to 80°). SAXS measurements (0.5 deg·min<sup>-1</sup>,  $2\theta$  ranging from 0 to 5°) were analyzed on an X-ray diffractometer (D8-Advance Bruker, Germany).<sup>50,51</sup> FTIR was conducted on a Frontier FTIR spectrometer (PerkinElmer, 400 cm<sup>-1</sup>  $\leq$  wavenumber  $\leq$  4000 cm<sup>-1</sup>).

**Preparation of Drug-Loaded Arg-MSNs.** To encapsulate the drug, BA (1.2 mg) and Arg-MSNs (0.4 mg) were fully dispersed in separate solutions of DMSO (1 mL) and then mixed and stirred under ultrasonic conditions in a water bath for 1 h. The suspension was subsequently washed three times by centrifugation at 13,000 rpm for 15 min to remove any residual DMSO, and then freeze-dried to produce Arg-MSNs@BA for further applications. For the preparation of fluorescently labeled Arg-MSNs, RhoB (*ex*: 546 nm, *em*: 610 nm),

and DiR (*ex*: 748 nm, *em*: 780 nm) were also loaded according to the above procedure, respectively.

The collected supernatant was used to evaluate the unloaded drug concentration using high-performance liquid chromatography (HPLC, Shimadzu, LC-20A20, Japan). The mobile phases used were acetonitrile/water (3:2, v/v) and 0.1% trifluoroacetic acid. The EE% and LC% of BA were calculated according to Formulas 1 and 2.

$$EE (\%) = \left( 1 - \frac{M_{en}}{M_{ad}} \right) \times 100\% \quad (1)$$

$$LC (\%) = \frac{M_{en}}{M_{total}} \times 100\% \quad (2)$$

where  $M_{en}$ ,  $M_{ad}$ , and  $M_{total}$  are the mass of encapsulated BA, added BA, and total Arg-MSNs@BA, respectively.

**Mesenchymal Stem Cell Membrane Isolation and M@Arg-MSNs@BA Preparation.** The BMSCs cells ( $1 \times 10^8$  per well) were suspended in a hypotonic lysing buffer (225 mM d-mannitol, 0.5% BSA (w/v), 75 mM sucrose, 0.5 mM EDTA, 30 mM Tris-HCl, protease inhibitors) at 4 °C for 1 h. After the indicated treatment, cells were lysed by repeated freezing (10 min each time) three times, thawed, and ultrasonicated for 5 min at 4 °C. The isolated membrane was obtained via low-temperature centrifugation at  $1 \times 10^4$  g for 20 min (for removing cell organelles) and then at  $1 \times 10^5$  g for 30 min (for collecting cell membranes). The obtained pellet was washed twice with prechilled 10 mM PBS containing protease inhibitors and resuspended in ultrapure water. The protein concentration was evaluated according to the procedures of BCA protein assay kit.

To obtain membrane-wrapped M@Arg-MSNs@BA, Arg-MSNs@BA aqueous solution was slowly added to BMSC membrane fragment aqueous solution under ultrasonic conditions at mass ratios (NPs weight: membrane protein weight) of 1:1, 1:2, 1:3, and 1:4 in a cold-water bath, and then the ultrasonic treatment was continued for 4 min. The product was stirred at 25 °C for 30 min and centrifuged at 13,000 rpm for 15 min to obtain M@Arg-MSNs@BA.

The membrane-wrapped M@Arg-MSNs@RhoB and M@Arg-MSNs@DiR were prepared according to the same procedure at a mass ratio (NP weight to membrane protein weight) of 1:4.

**Synthesis of DSPE-PEG-SLIGRL and Preparation of SL@M@Arg-MSNs@BA NPs.** DSPE-PEG<sub>2000</sub>-NHS (40 mg, 1.0 equiv) and 4-dimethylaminopyridine (DMAP) (5 mg, 3.0 equiv) were added to 10 mL of DMSO and stirred for 10 min. SL (10.64 mg, 1.0 equiv) was then added to the solution for a 48-h reaction at 25 °C. The product, DSPE-PEG-SLIGRL, was dialyzed for 72 h and subsequently freeze-dried. Subsequently, 200  $\mu$ L of DSPE-PEG-SLIGRL (1 mg·mL<sup>-1</sup>) was added to 2 mL of M@Arg-MSNs@BA (0.1 mg·mL<sup>-1</sup>). The mixture was continuously stirred at 25 °C for 30 min and then centrifuged at 13,000 rpm for 15 min to obtain SLIGRL@M@Arg-MSNs@BA. The SL@M@Arg-MSNs@RhoB and SL@M@Arg-MSNs@DiR were prepared according to the same procedure.

**Evaluation of Storage Stability and Trypsin-Sensitive Degradation of Arg-MSNs.** To determine the storage stability of Arg-MSNs@BA and SL@M@Arg-MSNs@BA, the particle size was monitored daily for 7 consecutive days while being stored at 25 °C. Besides, SL@M@Arg-MSNs@BA was incubated in a simulated physiological PBS (10 mM, pH 7.4) medium, while the particle size was detected for 7 consecutive days to determine their colloidal stability.

Arg-MSNs were immersed in PBS solutions (10 mM, pH 6.5) containing 60 and 120  $\mu$ g·mL<sup>-1</sup> of trypsin, respectively, and incubated at 37 °C for 0, 30, and 60 min. The responsiveness of the Arg-MSNs was assessed by the changes in the particle size, colloid state, and morphology, which were determined by the DLS, Tyndall light path photograph, and TEM image, respectively. Besides, after being incubated in PBS containing 60 and 120  $\mu$ g·mL<sup>-1</sup> of trypsin for 0, 0.5, 1, 3, 6, 9, 12, and 24 h, the suspension was centrifuged and the precipitate was subsequently redispersed by equal aqueous solution after sonication, while the changes in the UV spectrum were recorded on a NanoDrop instrument (Thermo).

**Trypsin-Responsive Drug-Release Profile of Arg-MSNs and SL@M@Arg-MSNs.** To evaluate the trypsin-triggered release profile of BA, the RhoB-loaded formulation was dispersed in a dialysis bag (Mw: 14,000 Da) and then immersed in the PBS medium containing 60, 300, and 600  $\mu$ g·mL<sup>-1</sup> trypsin. A sample (0.5 mL) was taken out of the medium solution at specified time points (0.5, 1, 3, 6, 9, and 12 h), while simultaneously adding the corresponding PBS medium (0.5 mL) containing trypsin. The amount of RhoB was measured using a microplate reader (Biotek SYNERGY H1).

**In Vitro Hemocompatibility Study.** The hemocompatibility of NPs was evaluated by quantifying the increased amount of free hemoglobin released from destructed erythrocyte destruction after being incubated with different concentrations of NPs (0–80  $\mu$ g·mL<sup>-1</sup>) for 4 h. 1% (w/v) Triton X-100 and PBS (10 mM, pH 7.4) were taken as positive and negative controls, respectively. The absorbance of the supernatant was measured at 576 nm using a microplate reader, and the rate of hemolysis was calculated using formula 3

$$\text{Hemolysis rate (\%)} = \frac{OD_{NPs} - OD_{PBS}}{OD_{Tx} - OD_{PBS}} \times 100\% \quad (3)$$

where  $OD_{NPs}$ ,  $OD_{Tx}$ , and  $OD_{PBS}$  are the absorbance of the supernatant from the group treated with various concentrations of NPs, Triton X-100, and PBS, respectively.

**Cell Study. Cell Culture.** AR42J were purchased from Procell Life Science Technology Co., Ltd. (Wuhan, China) and cultured in a cell culture flask (SAINING Biotechnology) containing F12 cell medium (BDBIO HangZhou China) with 1% penicillin–streptomycin and 20% fetal bovine serum (FBS, Procell) at 37 °C in 5% CO<sub>2</sub>. RAW264.7 cells were cultured in a DMEM/high-glucose medium (Sperikon Life Science & Biotechnology co., Ltd.) with 1% penicillin–streptomycin (H0518, Shanghai Chuanqiu Biotechnology Co., Ltd., China) and 10% FBS at 37 °C in 5% CO<sub>2</sub>.

**Assessment of Cellular Uptake Efficiency.** AR42J cells were seeded and cultured in a 20 mm confocal dish (NEST Biotechnology Co. Ltd.) at  $1 \times 10^4$  per dish. Then, the cells were incubated with Arg-MSNs@RhoB, M@Arg-MSNs@RhoB, and SL@M@Arg-MSNs@RhoB at a final RhoB concentration of 50  $\mu$ g·mL<sup>-1</sup> for predetermined time intervals (1, 3, 6, and 12 h). After washing the cells thrice, the nucleus was stained with DAPI (10  $\mu$ g·mL<sup>-1</sup>), respectively. After three washes, the cells were detected by confocal microscopy (Nikon, Japan). The average fluorescence intensity of RhoB in randomly selected visible images from different groups was quantified using ImageJ software.

**Cytosolic Calcium Level Measurements.** AR42J cells ( $1 \times 10^5$ ) were seeded and cultured in 12-well plates (SAINING Biotechnology). The cells were pretreated with TLCS (100 nmol·L<sup>-1</sup>) for 2 h to induce acute acinar cell injury, and then were incubated with PBS, free BA (400  $\mu$ g·mL<sup>-1</sup>), blank Arg-MSNs, Arg-MSNs@BA (400 ng·mL<sup>-1</sup>), M@Arg-MSNs@BA (400 ng·mL<sup>-1</sup>), and SL@Arg-MSNs@BA (100, 200, 400 ng·mL<sup>-1</sup>) for 12 h. Subsequently, the cells were collected, stained with Fluo-4-AM dye (2  $\mu$ mol·L<sup>-1</sup>) for 20 min, washed thrice, and suspended in PBS. For quantifying the intracellular calcium, the collected cells were detected by a flow cytometer (BD DxFLEX, American).

**Cell Viability Evaluation.** AR42J cells were cultured on a 96-well plate at  $1 \times 10^4$  cells per well and pretreated according to the above description (Section “Cytosolic calcium level measurements”). Then, the cell viability was measured using the CCK8 assay kit.<sup>52</sup>

**Macrophage Polarization Analysis.** The injured PACs were pretreated with TLCS (100 nmol·L<sup>-1</sup>) for 2 h. Then, cells were replaced with serum-free medium containing different formulations and then incubated for 12 h. After removing the serum-free medium containing different formulations and being incubated for another 12 h, the cell supernatant was collected and centrifuged to obtain PAC-derived conditioned medium, which was then added to RAW264.7 and incubated for an additional 12 h. To investigate the M1-type macrophage, the cells were fixed by paraformaldehyde for 30 min, blocked by a blocking solution containing 5% BSA/0.3% Triton X-

100 for 1 h, and then incubated with primary antibodies overnight at 4 °C, including CD68 (20  $\mu\text{g}\cdot\text{mL}^{-1}$ ), Arg-1 (5  $\mu\text{g}\cdot\text{mL}^{-1}$ ), and iNOS (5  $\mu\text{g}\cdot\text{mL}^{-1}$ )-specific antibodies.<sup>53</sup> Thereafter, the cells were incubated with the secondary antibody at 25 °C for 2 h and stained with DAPI. After three washes, the sections were imaged under an inverted fluorescence microscope (ICX41, SOPTOP, China). The average fluorescence intensity in randomly selected visible images from different groups was quantified using ImageJ software.

**Animal Study. Animals and Animal Study Approval.** ICR mice (male, 8 weeks) were fed a standard laboratory chow, water *ad libitum*, and housed in a specific pathogen-free (SPF) laboratory under a 12-h light/dark cycle at  $25 \pm 1$  °C. Animals were acclimatized for 1 week prior to the experiment. All animal experiments were approved by the Animal Research Committee of Ocean University of China and were performed in accordance with the principles of the care and use of laboratory animals.

**Establishment of Experimental AP Models.** The AP mouse model was established according to the methods previously reported. Briefly, mice were fasted for 12 h and had access to water *ad libitum* before induction of AP. The mouse was anesthetized and then positioned on a constant-temperature operating table (approximately  $37 \pm 1$  °C) (Beijing Zhongshi Dichuang Technology Development Co., Ltd.) to allow laparotomy (with a 1 cm longitudinal incision in the midline abdomen). The mice were then given a retrograde intraductal injection of 3.5% TLCS (w/v) at a speed of  $100 \mu\text{L}\cdot\text{min}^{-1}$ , while microarterial clamps were used to block the common bile duct and the opening site of the pancreatic duct during injection to prevent reflux to the liver and duodenum.<sup>54</sup> The abdomen of the mouse was closed, sutured, and sterilized again after removing the artery clamp and syringe. The Sham operation control group was anesthetized, underwent laparotomy, and was injected intraperitoneally with an equal volume of sterile saline.

**In Vivo Biodistribution.** TLCS-induced AP mice were randomly grouped and received intravenous injections (*i.v.*) of Arg-MSNs@DiR, M@Arg-MSNs@DiR, and SL@M@Arg-MSNs@DiR, respectively. Mice were euthanized on 1, 3, 6, 12, and 24 h after injection, while the major organs (heart, liver, spleen, lungs, kidneys, and pancreas) were collected for *ex vivo* imaging on a multifunctional fluorescence imaging system (VILBER Fusion FX7). The mean fluorescence intensity (MFI) in different formulations was semi-quantified to investigate the biodistribution of different formulations in AP mice.

**Evaluation of Cellular Targetability In Vivo.** The pancreatic tissue collected from the AP mice treated with Arg-MSNs@RhoB, M@Arg-MSNs@RhoB, and SL@M@Arg-MSNs@RhoB was mounted under optimal cutting temperature (OCT). Subsequently, these tissues were sectioned into 20- $\mu\text{m}$ -thick sections, fixed with 4% paraformaldehyde, and the nonspecific sites were then blocked by a blocking solution containing 5% BSA and 0.3% Triton X-100. The sections were then incubated with primary antibodies, including CD31 (10  $\mu\text{g}\cdot\text{mL}^{-1}$ , for labeling endothelial cells),  $\alpha$ -amylase (10  $\mu\text{g}\cdot\text{mL}^{-1}$ , for labeling PACs), CD68 (20  $\mu\text{g}\cdot\text{mL}^{-1}$ , for labeling macrophages), and CK19 (10  $\mu\text{g}\cdot\text{mL}^{-1}$ , for labeling ductal epithelial cells) at 4 °C overnight, and then exposed to the secondary antibodies for 2 h at 25 °C.<sup>55</sup> Nuclei were stained with DAPI. The image was obtained by confocal microscopy (Nikon, Japan). The localization of NPs in different types of cells can be expressed as the overlap between the RhoB fluorescence of the NPs and the corresponding fluorescence of cell markers.

**Animal Study Experimental Design.** The mice were randomly divided into six groups. (1) Sham operation group (control) ( $n = 8$ ); (2) model group: AP mice injected with sterile saline ( $n = 12$ ); (3) SL@M@Arg-MSNs group: AP mice injected with blank SL@M@Arg-MSNs ( $n = 12$ ); (4) low-dose SL@M@Arg-MSNs@BA group: AP mice injected with SL@M@Arg-MSNs@BA (BA:  $100 \mu\text{g}\cdot\text{kg}^{-1}$ ) ( $n = 12$ ); (5) middle-dose SL@M@Arg-MSNs@BA group: AP mice injected with SL@M@Arg-MSNs@BA (BA:  $200 \mu\text{g}\cdot\text{kg}^{-1}$ ) ( $n = 12$ ); and (6) high-dose SL@M@Arg-MSNs@BA group: AP mice injected with SL@M@Arg-MSNs@BA (BA:  $400 \mu\text{g}\cdot\text{kg}^{-1}$ ) ( $n = 12$ ).

The survival rate of mice was recorded and shown as a Kaplan–Meier curve. Blood samples were collected from the inner canthus vein at specific time points (6, 12, and 24 h) for biochemical analyses. After being euthanized, part of the pancreatic tissue of mice was fixed in 4% paraformaldehyde for histopathological examination and immunofluorescence examinations. The fresh pancreas sample was frozen and stored at  $-80$  °C for tissue homogenate index analysis and Western blotting analysis.

**Measurement of Serum  $\alpha$ -Amylase and Lipase Levels.** The blood samples were centrifuged (4000 rpm, 10 min) to obtain the supernatant. The serum amylase and lipase indicators were analyzed by the respective specific kits according to standard protocols.

**Pathological Observation.** Paraformaldehyde-fixed tissues were dehydrated, embedded in paraffin, sectioned into 4- $\mu\text{m}$ -thick sections, and dewaxed. Subsequently, the sections were stained with hematoxylin and eosin (H&E) dye and imaged using a Vectra automated quantitative pathology imaging system (PerkinElmer) for pathological observation.

**Antioxidant Activity Evaluation.** For superoxide level evaluation. Briefly, the fresh pancreatic tissue was embedded in the OCT medium, quickly frozen with liquid nitrogen, and cut into 5- $\mu\text{m}$ -thick sections with a cryostat microtome (Leica Biosystem, Germany). After that, the sections were directly stained with the DHE probe (1  $\text{mmol}\cdot\text{L}^{-1}$ ) and then stained with DAPI. After three washes, the sections were imaged under an inverted fluorescence microscope (ICX41, SOPTOP, China). In addition, the extent of oxidation-related components, including the lipid peroxidation product (MDA) and the antioxidant species (SOD and GSH), in tissue homogenates was determined by the respective specific kits according to standard protocols.

**TUNEL Assay.** The paraformaldehyde-fixed pancreatic tissue was dehydrated with 30% sucrose, embedded in the OCT medium, frozen, and cut into sections (5  $\mu\text{m}$ ) using a cryostat microtome. After being permeabilized with proteinase K for 10 min, the TUNEL labeling was executed in accordance with the guidelines provided by the manufacturer. The frozen section was then costained with DAPI. The number of TUNEL-positive cells was counted using ImageJ software, and the ratio of apoptosis was calculated using formula 4.

$$\text{Apoptosis cell ratio (\%)} = \frac{N_{\text{positive}}}{N_{\text{total}}} \times 100\% \quad (4)$$

where  $N_{\text{positive}}$  and  $N_{\text{total}}$  are the number of TUNEL-positive cells and the total number of cells.

**Immunofluorescence Staining.** Cryosections with 5  $\mu\text{m}$  thickness were further fixed in 4% paraformaldehyde and then incubated with a blocking solution containing 5% BSA and 0.3% Triton X-100 for blocking nonspecific sites. After that, the cryosections were incubated with primary antibody overnight at 4 °C, including CD31 (10  $\mu\text{g}\cdot\text{mL}^{-1}$ ), ICAM-1 (10  $\mu\text{g}\cdot\text{mL}^{-1}$ ), Ly6G (5  $\mu\text{g}\cdot\text{mL}^{-1}$ ), MPO (20  $\mu\text{g}\cdot\text{mL}^{-1}$ ), CitH3 (2  $\mu\text{g}\cdot\text{mL}^{-1}$ ), CD68 (20  $\mu\text{g}\cdot\text{mL}^{-1}$ ), iNOS (5  $\mu\text{g}\cdot\text{mL}^{-1}$ ), and Arg-1 (5  $\mu\text{g}\cdot\text{mL}^{-1}$ )-specific antibodies. After washing with PBS, it was incubated with the secondary antibody for 2 h at 25 °C. Subsequently, the cell nuclei were stained with DAPI. Finally, images were acquired through confocal microscopy (Nikon, Japan). The colocalization of the fluorescence signal in each plot was analyzed by Pearson's correlation coefficient using ImageJ software.<sup>56,57</sup>

**Western Blot Analysis.** Protein lysate from pancreatic tissue was prepared via homogenization in radioimmunoprecipitation assay (RIPA) lysis buffer containing the protease inhibitor cocktail (Sperikon Life Science & Biotechnology Co., Ltd.). The sample (approximately 30  $\mu\text{g}$  protein *per* sample) was loaded on a 12% polyacrylamide gel for electrophoretic separation and then transferred to a poly(vinylidene fluoride) (PVDF) membrane.<sup>58</sup> After being blocked with 5% BSA for 2 h, the PVDF membrane was incubated with primary antibodies of I $\kappa$ B $\alpha$  (1:1500), NF- $\kappa$ B (1:1500), TNF- $\alpha$  (1:500), IL-6 (1:500), MLKL (1:1000), p-MLKL (1:500), PIPK-3 (1:1000), p-PIPK-3 (1:500), cleaved caspase 9 (1:250), and cleaved caspase 8 (1:1000) at 4 °C overnight. Anti- $\beta$ -tubulin antibodies (1:2000) or anti-GADPH antibodies (1:2000) were used as loading

controls. After being labeled by the HRP-conjugated secondary antibody, the protein expression was visualized by an ECL Western blotting substrate, and immunoreactive band images were captured using a multiplex chemiluminescence gel imaging system (Tanon-5200Multi, Tanon, China). The protein expression level was analyzed by the integrated optical density after adjusting it to that of the corresponding internal reference protein calculated using ImageJ software. All data were obtained from three parallel experiments.

**In Vivo Safety Evaluation.** The serum ALT, AST, Cre, and BUN levels were detected in accordance with the instructions of the standard kit for measuring liver and kidney functions, respectively.<sup>59</sup> The major organs of AP mice with different formulation treatments were collected, fixed, sectioned, and stained with hematoxylin-eosin for pathological observation.

**Statistical Analysis.** The data are expressed as means  $\pm$  SEM. The statistical analysis was performed using one-way analysis of variance (ANOVA) with multiple comparisons.  $p < 0.05$  indicates that the difference is statistically significant (\* $p < 0.05$ , \*\* $p < 0.01$ , \*\*\* $p < 0.001$ , \*\*\*\* $p < 0.0001$ ).

## ASSOCIATED CONTENT

### Supporting Information

The Supporting Information is available free of charge at <https://pubs.acs.org/doi/10.1021/acsnano.4c05369>.

Formulation characterization, cellular uptake, cytoprotective evaluation, fluorescence imaging, and biocompatibility evaluation (PDF)

## AUTHOR INFORMATION

### Corresponding Author

**Zhiyu He** – *Frontiers Science Center for Deep Ocean Multispheres and Earth Systems, Key Laboratory of Marine Chemistry Theory and Technology, Ministry of Education/Sanya Oceanographic Institution, Ocean University of China, Qingdao/Sanya 266100/572024, China; Sanya Oceanographic Institution, Sanya 572024, China; College of Chemistry and Chemical Engineering, Ocean University of China, 266100 Qingdao, China; [orcid.org/0000-0002-4888-308X](https://orcid.org/0000-0002-4888-308X); Email: [hezhiyu@ouc.edu.cn](mailto:hezhiyu@ouc.edu.cn)*

### Authors

**Yanan Wang** – *Frontiers Science Center for Deep Ocean Multispheres and Earth Systems, Key Laboratory of Marine Chemistry Theory and Technology, Ministry of Education/Sanya Oceanographic Institution, Ocean University of China, Qingdao/Sanya 266100/572024, China; Sanya Oceanographic Institution, Sanya 572024, China; College of Chemistry and Chemical Engineering, Ocean University of China, 266100 Qingdao, China*

**Deyao Qian** – *Frontiers Science Center for Deep Ocean Multispheres and Earth Systems, Key Laboratory of Marine Chemistry Theory and Technology, Ministry of Education/Sanya Oceanographic Institution, Ocean University of China, Qingdao/Sanya 266100/572024, China; College of Chemistry and Chemical Engineering, Ocean University of China, 266100 Qingdao, China*

**Xinyuan Wang** – *Frontiers Science Center for Deep Ocean Multispheres and Earth Systems, Key Laboratory of Marine Chemistry Theory and Technology, Ministry of Education/Sanya Oceanographic Institution, Ocean University of China, Qingdao/Sanya 266100/572024, China; College of Chemistry and Chemical Engineering, Ocean University of China, 266100 Qingdao, China*

**Xue Zhang** – *Frontiers Science Center for Deep Ocean Multispheres and Earth Systems, Key Laboratory of Marine Chemistry Theory and Technology, Ministry of Education/Sanya Oceanographic Institution, Ocean University of China, Qingdao/Sanya 266100/572024, China; College of Chemistry and Chemical Engineering, Ocean University of China, 266100 Qingdao, China*

**Zerui Li** – *Frontiers Science Center for Deep Ocean Multispheres and Earth Systems, Key Laboratory of Marine Chemistry Theory and Technology, Ministry of Education/Sanya Oceanographic Institution, Ocean University of China, Qingdao/Sanya 266100/572024, China; College of Chemistry and Chemical Engineering, Ocean University of China, 266100 Qingdao, China*

**Xinlei Meng** – *Frontiers Science Center for Deep Ocean Multispheres and Earth Systems, Key Laboratory of Marine Chemistry Theory and Technology, Ministry of Education/Sanya Oceanographic Institution, Ocean University of China, Qingdao/Sanya 266100/572024, China; College of Chemistry and Chemical Engineering, Ocean University of China, 266100 Qingdao, China*

**Liangmin Yu** – *Frontiers Science Center for Deep Ocean Multispheres and Earth Systems, Key Laboratory of Marine Chemistry Theory and Technology, Ministry of Education/Sanya Oceanographic Institution, Ocean University of China, Qingdao/Sanya 266100/572024, China; Sanya Oceanographic Institution, Sanya 572024, China; College of Chemistry and Chemical Engineering, Ocean University of China, 266100 Qingdao, China*

**Xuefeng Yan** – *Frontiers Science Center for Deep Ocean Multispheres and Earth Systems, Key Laboratory of Marine Chemistry Theory and Technology, Ministry of Education/Sanya Oceanographic Institution, Ocean University of China, Qingdao/Sanya 266100/572024, China; College of Chemistry and Chemical Engineering, Ocean University of China, 266100 Qingdao, China*

Complete contact information is available at: <https://pubs.acs.org/doi/10.1021/acsnano.4c05369>

### Author Contributions

<sup>†</sup>Y.W. and D.Q. contributed equally to this perspective paper.

### Notes

The authors declare no competing financial interest.

## ACKNOWLEDGMENTS

This work was financially supported by the Taishan Scholar Foundation of Shandong Province [No. tsqn202211065], the Sanya Yazhou Bay Science and Technology City [No. 2021JLH0037], and the Hainan Province Science and Technology Special Fund [ZDYF2024SHFZ056].

## REFERENCES

- (1) Boxhoorn, L.; Voermans, R. P.; Bouwense, S. A.; Bruno, M. J.; Verdonk, R. C.; Boermeester, M. A.; van Santvoort, H. C.; Besselink, M. G. Acute Pancreatitis. *Lancet* **2020**, 396 (10252), 726–734.
- (2) Gardner, T. B. Acute Pancreatitis. *Ann. Int. Med.* **2021**, 174 (2), ITC17–ITC32.
- (3) Mederos, M. A.; Reber, H. A.; Girgis, M. D. Acute Pancreatitis. *JAMA* **2021**, 325 (4), 382–390.
- (4) de-Madaria, E.; Buxbaum, J. L. Advances in the Management of Acute Pancreatitis. *Nat. Rev. Gastroenterol. Hepatol.* **2023**, 20 (11), 691–692.

- (5) Li, X. W.; Wang, C. H.; Dai, J. W.; Tsao, S. H.; Wang, P. H.; Tai, C. C.; Chien, R. N.; Shao, S. C.; Lai, E. C. C. Comparison of Clinical Outcomes between Aggressive and Non-Aggressive Intravenous Hydration for Acute Pancreatitis: a Systematic Review and Meta-Analysis. *Crit. Care* **2023**, *27* (1), No. 122.
- (6) Lee, P. J.; Papachristou, G. I. New Insights into Acute Pancreatitis. *Nat. Rev. Gastroenterol. Hepatol.* **2019**, *16* (8), 479–496.
- (7) Mukherjee, R.; Mareninova, O. A.; Odinkova, I. V.; Huang, W.; Murphy, J.; Chvanov, M.; Javed, M. A.; Wen, L.; Booth, D. M.; Cane, M. C.; Awais, M.; Gavillet, B.; Pruss, R. M.; Schaller, S.; Molkenkin, J. D.; Tepikin, A. V.; Petersen, O. H.; Pandol, S. J.; Gukovsky, I.; Criddle, D. N.; et al. Mechanism of Mitochondrial Permeability Transition Pore Induction and Damage in the Pancreas: Inhibition Prevents Acute Pancreatitis by Protecting Production of ATP. *Gut* **2016**, *65* (8), 1333–1346.
- (8) Du, W.; Liu, G.; Shi, N.; Tang, D.; Ferdek, P. E.; Jakubowska, M. A.; Liu, S.; Zhu, X.; Zhang, J.; Yao, L.; Sang, X.; Zou, S.; Liu, T.; Mukherjee, R.; Criddle, D. N.; Zheng, X.; Xia, Q.; Berggren, P. O.; Huang, W.; Sutton, R.; et al. A MicroRNA Checkpoint for Ca<sup>2+</sup> Signaling and Overload in Acute Pancreatitis. *Mol. Ther.* **2022**, *30* (4), 1754–1774.
- (9) Takano, T.; Yule, D. I. Ca<sup>2+</sup> Signals in Pancreatic Acinar Cells in Response to Physiological Stimulation *in vivo*. *J. Physiol.* **2023**, *601* (12), 2391–2405.
- (10) Zi, Z.; Rao, Y. Discoveries of GPR39 as an Evolutionarily Conserved Receptor For Bile Acids and of Its Involvement in Biliary Acute Pancreatitis. *Sci. Adv.* **2024**, *10* (5), No. eadj0146.
- (11) Hu, Q.; Yao, J.; Wu, X.; Li, J.; Li, G.; Tang, W.; Liu, J.; Wan, M. Emodin Attenuates Severe Acute Pancreatitis-Associated Acute Lung Injury by Suppressing Pancreatic Exosome-Mediated Alveolar Macrophage Activation. *Acta Pharm. Sin. B* **2022**, *12* (10), 3986–4003.
- (12) Li, H.; Xie, J.; Guo, X.; Yang, G.; Cai, B.; Liu, J.; Yue, M.; Tang, Y.; Wang, G.; Chen, S.; Guo, J.; Qi, X.; Wang, D.; Zheng, H.; Liu, W.; Yu, H.; Wang, C.; Zhu, S. J.; Guo, F. *Bifidobacterium spp.* and their Metabolite Lactate Protect Against Acute Pancreatitis via Inhibition of Pancreatic and Systemic Inflammatory Responses. *Gut Microbes* **2022**, *14* (1), No. 2127456.
- (13) Sun, S.; Lv, W.; Li, S.; Zhang, Q.; He, W.; Min, Z.; Teng, C.; Chen, Y.; Liu, L.; Yin, J.; Zhu, B.; Xu, M.; Dai, D.; Xin, H. Smart Liposomal Nanocarrier Enhanced the Treatment of Ischemic Stroke through Neutrophil Extracellular Traps and Cyclic Guanosine Monophosphate-Adenosine Monophosphate Synthase-Stimulator of Interferon Genes (cGAS-STING) Pathway Inhibition of Ischemic Penumbra. *ACS Nano* **2023**, *17* (18), 17845–17857.
- (14) Hutchinson, J. P.; Rowland, P.; Taylor, M. R. D.; Christodoulou, E. M.; Haslam, C.; Hobbs, C. L.; Holmes, D. S.; Homes, P.; Liddle, J.; Mole, D. J.; Uings, I.; Walker, A. L.; Webster, S. P.; Mowat, C. G.; Chung, C. W. Structural and Mechanistic Basis of Differentiated Inhibitors of the Acute Pancreatitis Target Kynurenine-3-Monooxygenase. *Nat. Commun.* **2017**, *8* (1), No. 15827.
- (15) Cai, Y.; Cao, Q.; Li, J.; Liu, T. Targeting and Functional Effects of Biomaterials-Based Nanoagents for Acute Pancreatitis Treatment. *Front. Bioeng. Biotechnol.* **2023**, *10*, No. 1122619.
- (16) Zhang, Q.; Li, S.; Yu, Y.; Zhu, Y.; Tong, R. A Mini-Review of Diagnostic and Therapeutic Nano-Tools for Pancreatitis. *Int. J. Nanomed.* **2022**, *Volume 17*, 4367.
- (17) Zhang, Q.; Zhou, J.; Zhou, J.; Fang, R. H.; Gao, W.; Zhang, L. Lure-and-Kill Macrophage Nanoparticles Alleviate the Severity of Experimental Acute Pancreatitis. *Nat. Commun.* **2021**, *12* (1), No. 4136.
- (18) Yao, Q.; Jiang, X.; Zhai, Y. Y.; Luo, L. Z.; Xu, H. L.; Xiao, J.; Kou, L.; Zhao, Y. Z. Protective Effects and Mechanisms of Bilirubin Nanomedicine against Acute Pancreatitis. *J. Controlled Release* **2020**, *322*, 312–325.
- (19) Chen, K.; Zhang, Z.; Fang, Z.; Zhang, J.; Liu, Q.; Dong, W.; Liu, Y.; Wang, Y.; Wang, J. Aged-Signal-Eliciting Nanoparticles Stimulated Macrophage-Mediated Programmed Removal of Inflammatory Neutrophils. *ACS Nano* **2023**, *17* (14), 13903–13916.
- (20) Mei, Q.; Deng, G.; Huang, Z.; Yin, Y.; Li, C.; Hu, J.; Fu, Y.; Wang, X.; Zeng, Y. Porous COS@SiO<sub>2</sub> Nanocomposites Ameliorate Severe Acute Pancreatitis and Associated Lung Injury by Regulating the Nr1f2 Signaling Pathway in Mice. *Front. Chem.* **2020**, *8*, 720.
- (21) Lin, W.; Zhao, X. Y.; Cheng, J. W.; Li, L. T.; Jiang, Q.; Zhang, Y. X.; Han, F. Signaling Pathways in Brain Ischemia: Mechanisms and Therapeutic Implications. *Pharmacol. Ther.* **2023**, *251*, No. 108541.
- (22) Jing, F.; Zhu, Y.; Li, F.; Wang, Y.; Yu, X.; Zhang, K.; Xin, G.; Huang, W. Bimetallic Ions-Doped Carbon Dots Nanotheranostics for Imaging-Guided Macrophage Polarization/ROS Scavenging in Acute Pancreatitis. *Chem. Eng. J.* **2023**, *465*, No. 142675.
- (23) Liu, L.; Zhang, Y.; Li, X.; Deng, J. Microenvironment of Pancreatic Inflammation: Calling for Nanotechnology for Diagnosis and Treatment. *J. Nanobiotechnol.* **2023**, *21* (1), No. 443.
- (24) Hu, Z.; Wang, D.; Gong, J.; Li, Y.; Ma, Z.; Luo, T.; Jia, X.; Shi, Y.; Song, Z. MSCs Deliver Hypoxia-Treated Mitochondria Reprogramming Acinar Metabolism to Alleviate Severe Acute Pancreatitis Injury. *Adv. Sci.* **2023**, *10* (25), No. 2207691.
- (25) Vandermarliere, E.; Mueller, M.; Martens, L. Getting Intimate with Trypsin, the Leading Protease in Proteomics. *Mass Spectrom. Rev.* **2013**, *32* (6), 453–465.
- (26) Ahmed Al-Hadhrani, N.; Ladwig, A.; Rahman, A.; Rozas, I.; Paul, G.; Malthouse, J.; Evans, P. Synthesis of 2-Guanidiny Pyridines and their Trypsin Inhibition and Docking. *Bioorg. Med. Chem.* **2020**, *28* (16), No. 115612.
- (27) Xu, B.; Li, S.; Shi, R.; Liu, H. Multifunctional Mesoporous Silica Nanoparticles for Biomedical Applications. *Signal Transduction Targeted Ther.* **2023**, *8* (1), No. 435.
- (28) Shao, D.; Li, M.; Wang, Z.; Zheng, X.; Lao, Y. H.; Chang, Z.; Zhang, F.; Lu, M.; Yue, J.; Hu, H.; Yan, H.; Chen, L.; Dong, W.; Leong, K. W. Bioinspired Diselenide-Bridged Mesoporous Silica Nanoparticles for Dual-Responsive Protein Delivery. *Adv. Mater.* **2018**, *30* (29), No. 1801198.
- (29) Pinese, C.; Lin, J.; Milbreta, U.; Li, M.; Wang, Y.; Leong, K. W.; Chew, S. Y. Sustained Delivery of siRNA/Mesoporous Silica Nanoparticle Complexes from Nanofiber Scaffolds for Long-Term Gene Silencing. *Acta Biomater.* **2018**, *76*, 164–177.
- (30) Li, M.; Lao, Y. H.; Mintz, R. L.; Chen, Z.; Shao, D.; Hu, H.; Wang, H. X.; Tao, Y.; Leong, K. W. A Multifunctional Mesoporous Silica–Gold Nanocluster Hybrid Platform for Selective Breast Cancer Cell Detection Using a Catalytic Amplification-Based Colorimetric Assay. *Nanoscale* **2019**, *11* (6), 2631–2636.
- (31) Zhang, W.; Kan, Q.; Chen, L.; Xie, L.; Cui, M.; Xi, Z.; Xi, Y.; Li, S.; Xu, L. Preparation and Application of Mesoporous Core-Shell Nanosilica Using Leucine Derivative as Template in Effective Drug Delivery. *Chin. Chem. Lett.* **2020**, *31* (5), 1165–1167.
- (32) Sun, J.; Li, J.; Li, X.; Yang, L.; Liu, Y.; Gao, H.; Xiang, L. Sequentially Responsive Size Reduction and Drug Release of Core-Satellite Nanoparticles to Enhance Tumor Penetration and Effective Tumor Suppression. *Chin. Chem. Lett.* **2023**, *34* (5), No. 107891.
- (33) Jin, S.; Orabi, A. I.; Le, T.; Javed, T. A.; Sah, S.; Eisses, J. F.; Bottino, R.; Molkenkin, J. D.; Husain, S. Z. Exposure to Radiocontrast Agents Induces Pancreatic Inflammation by Activation of Nuclear Factor- $\kappa$ B, Calcium Signaling, and Calcineurin. *Gastroenterology* **2015**, *149* (3), 753–764.
- (34) Wang, Y.; Pu, M.; Yan, J.; Zhang, J.; Wei, H.; Yu, L.; Yan, X.; He, Z. 1,2-Bis(2-aminophenoxy)ethane-N,N,N',N'-tetraacetic Acid Acetoxymethyl Ester Loaded Reactive Oxygen Species Responsive Hyaluronic Acid–Bilirubin Nanoparticles for Acute Kidney Injury Therapy via Alleviating Calcium Overload Mediated Endoplasmic Reticulum Stress. *ACS Nano* **2023**, *17* (1), 472–491.
- (35) Quarato, G.; Llambi, F.; Guy, C. S.; Min, J.; Actis, M.; Sun, H.; Narina, S.; Pruet-Miller, S. M.; Peng, J.; Rankovic, Z.; Green, D. R. Ca<sup>2+</sup>-Mediated Mitochondrial Inner Membrane Permeabilization Induces Cell Death Independently of Bax and Bak. *Cell Death Differ.* **2022**, *29* (7), 1318–1334.
- (36) Raraty, M.; Ward, J.; Erdemli, G.; Vaillant, C.; Neoptolemos, J. P.; Sutton, R.; Petersen, O. H. Calcium-Dependent Enzyme Activation and Vacuole Formation in the Apical Granular Region of

- Pancreatic Acinar Cells. *Proc. Natl. Acad. Sci. U.S.A.* **2000**, *97* (24), 13126–13131.
- (37) Wang, Y.; Wang, X.; Zhang, X.; Zhang, B.; Meng, X.; Qian, D.; Xu, Y.; Yu, L.; Yan, X.; He, Z. Inflammation and Acinar Cell Dual-Targeting Nanomedicines for Synergistic Treatment of Acute Pancreatitis via  $\text{Ca}^{2+}$  Homeostasis Regulation and Pancreas Autodigestion Inhibition. *ACS Nano* **2024**, *18* (18), 11778–11803.
- (38) Wang, Y.; Wei, H.; Li, K.; Liu, L.; Zhu, Y.; Wang, X.; Yan, J.; Yu, L.; Yan, X.; He, Z. Ros-Responsive Dextran-Phenylboronic Acid-Silibinin Nanoparticles for Targeting Delivery of BAPTA-AM to Effectively Eliminate Calcium Overload-Mediated Inflammatory Cascades and Mitochondrial Apoptosis: Alleviating Acute Liver Injury. *Chem. Eng. J.* **2024**, *480*, No. 148283.
- (39) Xiao, Y.; Xu, R. H.; Dai, Y. Nanoghosts: Harnessing Mesenchymal Stem Cell Membrane for Construction of Drug Delivery Platforms via Optimized Biomimetics. *Small* **2023**, *20* (1), No. 2304824.
- (40) Fan, L.; Wei, A.; Gao, Z.; Mu, X. Current Progress of Mesenchymal Stem Cell Membrane-Camouflaged Nanoparticles for Targeted Therapy. *Biomed. Pharmacother.* **2023**, *161*, No. 114451.
- (41) Liu, H.; Miao, Z.; Zha, Z. Cell Membrane-Coated Nanoparticles for Immunotherapy. *Chin. Chem. Lett.* **2022**, *33* (4), 1673–1680.
- (42) Dogra, P.; Adolphi, N. L.; Wang, Z.; Lin, Y.-S.; Butler, K. S.; Durfee, P. N.; Croissant, J. G.; Nouredine, A.; Coker, E. N.; Bearer, E. L.; Cristini, V.; Brinker, C. J. Establishing the Effects of Mesoporous Silica Nanoparticle Properties on *in vivo* Disposition Using Imaging-Based Pharmacokinetics. *Nat. Commun.* **2018**, *9* (1), No. 4551.
- (43) Singh, V. P.; Bhagat, L.; Navina, S.; Sharif, R.; Dawra, R. K.; Saluja, A. K. Protease-Activated Receptor-2 Protects Against Pancreatitis by Stimulating Exocrine Secretion. *Gut* **2007**, *56* (7), 958–964.
- (44) Song, Z.; Zhu, Q.; Zhang, Y.; Yan, X.; Pan, X. Ascites Volume Quantification via Abdominal CT: A Novel Approach to Predict Severity in Acute Pancreatitis. *Med. Sci. Monit.* **2023**, *29*, No. e940783.
- (45) Bush, N.; Rana, S. S. Ascites in Acute Pancreatitis: Clinical Implications and Management. *Dig. Dis. Sci.* **2022**, *67* (6), 1987–1993.
- (46) Samanta, J.; Rana, A.; Dhaka, N.; Agarwala, R.; Gupta, P.; Sinha, S. K.; Gupta, V.; Yadav, T. D.; Kochhar, R. Ascites in Acute Pancreatitis: Not a Silent Bystander. *Pancreatol.* **2019**, *19* (5), 646–652.
- (47) Xu, Q.; Shi, M.; Ding, L.; Xia, Y.; Luo, L.; Lu, X.; Zhang, X.; Deng, D. Y. B. High Expression of P-Selectin Induces Neutrophil Extracellular Traps via the PSGL-1/Syk/ $\text{Ca}^{2+}$ /PAD4 Pathway to Exacerbate Acute Pancreatitis. *Front. Immunol.* **2023**, *14*, No. 1265344.
- (48) Zhang, J.; Tang, K.; Liu, Z.; Zhang, Z.; Duan, S.; Wang, H.; Yang, H.; Yang, D.; Fan, W. Tumor Microenvironment-Responsive Degradable Silica Nanoparticles: Design Principles and Precision Theranostic Applications. *Nanoscale Horiz.* **2024**, *9* (2), 186–214.
- (49) Zhang, J.; Zhou, J.; Tang, L.; Ma, J.; Wang, Y.; Yang, H.; Wang, X.; Fan, W. Custom-Design of Multi-Stimuli-Responsive Degradable Silica Nanoparticles for Advanced Cancer-Specific Chemotherapy. *Small* **2024**, No. 2400353.
- (50) Hu, Q.; Qi, S.; Huo, Q.; Zhao, Y.; Sun, J.; Chen, X.; Lv, M.; Zhou, W.; Feng, C.; Chai, X.; Yang, H.; He, C. Designing Efficient Nitrate Reduction Electrocatalysts by Identifying and Optimizing Active Sites of Co-Based Spinels. *J. Am. Chem. Soc.* **2024**, *146* (5), 2967–2976.
- (51) Hu, Q.; Zhou, W.; Qi, S.; Huo, Q.; Li, X.; Lv, M.; Chen, X.; Feng, C.; Yu, J.; Chai, X.; Yang, H.; He, C. Pulsed Co-Electrolysis of Carbon Dioxide and Nitrate for Sustainable Urea Synthesis. *Nat. Sustainability* **2024**, *7*, 442–451.
- (52) Wang, Y.; Li, Q.; Deng, M.; Chen, K.; Wang, J. Self-Assembled Metal-Organic Frameworks Nanocrystals Synthesis and Application for Plumbagin Drug Delivery in Acute Lung Injury Therapy. *Chin. Chem. Lett.* **2022**, *33* (1), 324–327.
- (53) Park, J. V.; Chandra, R.; Cai, L.; Ganguly, D.; Li, H.; Toombs, J. E.; Girard, L.; Brekken, R. A.; Minna, J. D. Tumor Cells Modulate Macrophage Phenotype in a Novel *in vitro* Co-Culture Model of the NSCLC Tumor Microenvironment. *J. Thorac. Oncol.* **2022**, *17* (10), 1178–1191.
- (54) Zhu, Q.; Yuan, C.; Dong, X.; Wang, Y.; Li, B.; Tu, B.; Chen, W.; Xu, X.; Gong, W.; Xiao, W.; Ding, Y.; Hu, L.; Li, W.; Lu, G. Bile Acid Metabolomics Identifies Chenodeoxycholic Acid as a Therapeutic Agent for Pancreatic Necrosis. *Cell Rep. Med.* **2023**, *4* (12), No. 101304, DOI: 10.1016/j.xcrm.2023.101304.
- (55) Kou, X.; Liu, J.; Wang, D.; Yu, M.; Li, C.; Lu, L.; Chen, C.; Liu, D.; Yu, W.; Yu, T.; Liu, Y.; Mao, X.; Najji, A.; Cai, T.; Sun, L.; Shi, S. Exocrine Pancreas Regeneration Modifies Original Pancreas to Alleviate Diabetes in Mouse Models. *Sci. Transl. Med.* **2022**, *14* (656), No. eabg9170.
- (56) Lincoln, R.; Bossi, M. L.; Rimmel, M.; D’Este, E.; Butkevich, A. N.; Hell, S. W. A General Design of Caging-Group-Free Photo-activatable Fluorophores for Live-Cell Nanoscopy. *Nat. Chem.* **2022**, *14* (9), 1013–1020.
- (57) Cheng, B.; Cao, L.; Li, C.; Huo, F. Y.; Meng, Q. F.; Tong, G.; Wu, X.; Bu, L. L.; Rao, L.; Wang, S. Fluorine-Doped Carbon Quantum Dots with Deep-Red Emission for Hypochlorite Determination and Cancer Cell Imaging. *Chin. Chem. Lett.* **2024**, *35* (6), No. 108969.
- (58) Wei, H.; Li, X.; Huang, F.; Wu, S.; Ding, H.; Chen, Q.; Li, M.; Lang, X. Red Light-Driven Generation of Reactive Oxygen Species for the Targeted Oxidation of Glioma Cells and Thiols over Covalent Organic Framework. *Chin. Chem. Lett.* **2023**, *34* (12), No. 108564.
- (59) Wang, Y.; Song, X.; Zhuang, L.; Lang, H.; Yu, L.; Yan, X.; He, Z. Kinetic Control of Phytic Acid/Lixisenatide/Fe (III) Ternary Nanoparticles Assembly Process for Sustained Peptide Release. *Int. J. Pharm.* **2022**, *611*, No. 121317.